JCB Journal of Cell Biology

REPORT

Long lifetime and tissue-specific accumulation of lamin A/C in Hutchinson–Gilford progeria syndrome

John Hasper[1], Kevin Welle[2], Kyle Swovick[2], Jennifer Hryhorenko[2], Sina Ghaemmaghami[2,3], and Abigail Buchwalter[1,4]

***LMNA* mutations cause laminopathies that afflict the cardiovascular system and include Hutchinson-Gilford progeria syndrome. The origins of tissue specificity in these diseases are unclear as the lamin A/C proteins are broadly expressed. We show that *LMNA* transcript levels are not predictive of lamin A/C protein levels across tissues and use quantitative proteomics to discover that tissue context and disease mutation each influence lamin A/C protein's lifetime. Lamin A/C's lifetime is an order of magnitude longer in the aorta, heart, and fat, where laminopathy pathology is apparent, than in the liver and intestine, which are spared from the disease. Lamin A/C is especially insoluble in cardiovascular tissues, which may limit degradation and promote protein stability. Progerin is even more long lived than lamin A/C in the cardiovascular system and accumulates there over time. Progerin accumulation is associated with impaired turnover of hundreds of abundant proteins in progeroid tissues. These findings identify impaired lamin A/C protein turnover as a novel feature of laminopathy syndromes.**

Introduction

The nuclear lamina is an intermediate filament meshwork that underlies the nuclear envelope. In mammals, this structure is composed of "A-type" (lamins A and C) and "B-type" (lamins B1 and B2) lamin proteins, which assemble into bundled filaments that strengthen the nucleus and scaffold the genome.

The *LMNA* locus encodes the lamin A and C proteins and is a hotspot for mutations that have been linked to at least 15 distinct syndromes referred to as "laminopathies" (Schreiber and Kennedy, 2013). While the lamin A/C proteins are broadly expressed, laminopathies primarily afflict the cardiovascular system, muscle, bone, and fat (Schreiber and Kennedy, 2013). Hutchinson-Gilford progeria syndrome (HGPS) is a rare and devastating autosomal dominant laminopathy that resembles physiological aging at an accelerated rate, with rapid deterioration of the skin, adipose tissue, and cardiovascular system. Most cases of HGPS are caused by a single base pair substitution (GGC > GGT) that activates a cryptic splice site, resulting in the in-frame deletion of a portion of exon 11 in *LMNA* and the production of a toxic, dominant negative "progerin" protein.

Several gene therapy approaches have recently been tested in mouse models of HGPS, ranging from disrupting the mutant allele with CRISPR/Cas9 indels (Beyret et al., 2019; Santiago-Fernández et al., 2019), correcting the mutation with base editing (Koblan et al., 2021), or interfering with the RNA splicing event that produces the *progerin* transcript (Osorio et al., 2011; Puttaraju et al., 2021; Scaffidi and Misteli, 2005; Erdos et al., 2021). Because HGPS is caused by the toxic effects of a dominant negative protein, an effective gene therapy will need to induce the removal of as much of the progerin protein as possible. However, gene therapies have variable effects on progerin protein levels in vivo; for instance, in treatment regimes that effectively clear the mutant protein from the liver, the protein persists to some extent in the cardiovascular system (Beyret et al., 2019; Puttaraju et al., 2021; Koblan et al., 2021; Erdos et al., 2021; Osorio et al., 2011; Santiago-Fernández et al., 2019). In one particularly striking case, high levels of progerin protein were found to persist in the heart after over 5 mo of treatment with splice-interfering antisense oligonucleotides, long after the transcript had been depleted (Puttaraju et al., 2021).

Why is progerin so intractable to remove in the cardiovascular system? Progerin could be produced in high amounts in these tissues, which express high levels of lamin A/C (Swift et al., 2013). A second, non-exclusive possibility is that progerin is especially long-lived in the cardiovascular system. The B-type lamins have extremely long lifetimes of months to years in the nervous system (Toyama et al., 2013; Razafsky et al., 2016), but the lifetimes of the A-type lamins within tissues have not been defined. We previously profiled protein lifetimes in cultured fibroblasts and found no evidence that the HGPS-causative mutation impairs the turnover of lamin A/C (Buchwalter

---

[1]Cardiovascular Research Institute, University of California, San Francisco, CA, USA; [2]Mass Spectrometry Resource Laboratory, University of Rochester, Rochester, NY, USA; [3]Department of Biology, University of Rochester, Rochester, NY, USA; [4]Department of Physiology, University of California, San Francisco, CA, USA.

Correspondence to Abigail Buchwalter: abigail.buchwalter@ucsf.edu.

https://doi.org/10.1083/jcb.202307049

and Hetzer, 2017). However, these experiments could not address the potential influence of tissue context on the turnover rate of these proteins.

Here, we deploy our recently developed dynamic proteomic approach, turnover and replication analysis by isotope labeling (TRAIL; Hasper et al., 2023) to define the turnover rate of the lamin A/C and progerin proteins within tissues of healthy and progeroid mice. We report that lamin A/C turns over an order of magnitude more slowly within disease-afflicted tissues compared with disease-spared tissues. Further, we show that the progerin mutant is even more long-lived than wild-type lamin A/C in the cardiovascular system, leading us to estimate a months-long lifetime of this toxic protein in these diseased tissues. These findings have major implications for both the pathogenesis and treatment of laminopathies and establish a novel paradigm of rare diseases caused by the action of long-lived mutant proteins.

Results and discussion

High expression of lamin A/C/progerin proteins across tissues

High progerin abundance could both drive disease and thwart gene therapies. We reasoned that tissues that express high levels of lamin A/C in healthy individuals may also express more progerin in diseased individuals, and we mined a quantitative proteomic atlas of 29 human tissues (Wang et al., 2019) to evaluate the relationship between lamin A/C protein expression and laminopathy pathology. These data indicate that the lamin A/C proteins are extremely abundant in human smooth muscle (Fig. 1 A), consistent with previous reports in mouse tissues (Kim et al., 2018; Swift et al., 2013). Because vascular smooth muscle is prominently affected in HGPS (Varga et al., 2006; Hamczyk et al., 2018), these data could suggest that high lamin A/C abundance correlates with disease vulnerability. However, the heart and adipose tissue are also afflicted in HGPS and other laminopathies, but these tissues express lamin A/C at a level comparable with many unaffected tissues (Fig. 1 A). In fact, 26 of the 29 analyzed tissues are estimated to produce >10^7 copies of lamin A/C per cell (Fig. S1 A), indicating that high expression levels of lamin A/C are not sufficient to drive disease.

The abundance ratio of the A-type to B-type lamins influences nuclear mechanics (Swift et al., 2013) and it has been proposed that tissues where this ratio is highest might be most sensitive to *LMNA* mutations (Kim et al., 2018). Consistent with previous analyses in the mouse (Kim et al., 2018), the ratio of A-type:B-type lamins is very high in the human heart (~9:1), smooth muscle (~7:1), and fat (~4:1; Fig. S1 D). However, this ratio is comparably high in many unaffected tissues (Fig. S1 D). Therefore, a high ratio of A-type to B-type lamins cannot explain why some tissues are more vulnerable to *LMNA* mutations.

We next considered the alternative possibility that progerin abundance varies independently of lamin A/C abundance across diseased tissues. The genetic lesion that causes HGPS activates a cryptic splice site, resulting in the in-frame deletion of a portion of exon 11 in *LMNA* without altering the shorter *LMNC* isoform (Fig. 1 B). Variable use of this splice site can produce either *Progerin* or *LMNA* from the mutant allele and could modulate *Progerin* production across tissues (Reddel and Weiss, 2004). To explore this possibility, we turned to a genetically modified mouse model that harbors the HGPS-causative C>T substitution in the endogenous mouse *Lmna* locus (*Lmna*^{G609G}; Osorio et al., 2011). We focused our analyses on heterozygous mice (*Lmna*$^{G609G/+}$), which succumb to the disease between 9 and 12 mo of age (Osorio et al., 2011).

We evaluated the proportional abundance of the lamin A, lamin C, and progerin proteins by Western blotting in progeroid mouse tissues (Fig. 1, C and D) using an antibody that detects an epitope shared across all A-type lamins (see Materials and methods). We reasoned that this approach was the most relevant way to quantify the dose of progerin as the ratio of progerin to wild-type lamin A/C has been proposed to influence pathology (Kim et al., 2018). We found that progerin contributes up to 50% of the total amount of A-type lamins detected in tissues (Fig. 1, C and D), but the proportional abundance of progerin does not correlate with pathology; the disease variant is highly abundant in afflicted tissues, such as the aorta and adipose tissue, as well as in tissues that remain more functional, such as the kidney and large intestine. Altogether, these analyses indicate that protein abundance alone cannot explain either the vulnerability of specific tissues to *LMNA* mutations or the resistance of progerin to therapeutic interventions.

Lamin A/C/progerin protein and transcript levels are poorly correlated across tissues

What other factors could modulate both the responsiveness of progerin to treatment and the effects of progerin on a tissue? One potential influence could be the lifetime of the lamin A/C/progerin proteins. A protein's lifetime reflects its rates of synthesis and degradation; short-lived proteins are frequently renewed, while long-lived proteins can persist for weeks or even months within mammalian tissues (Toyama et al., 2013). Because long-lived proteins are rarely synthesized and rarely degraded, their abundance may be poorly sensitive to changes in their transcript levels. To explore the relationship between *LMNA* transcript and lamin A/C protein abundance, we compared matched RNAseq and proteomic data across 29 human tissues (Wang et al., 2019). This analysis revealed that *LMNA* transcript and lamin A/C protein abundances are uncorrelated (Fig. 1 E, r^2 ~0). For comparison, the enzyme SYK has well-correlated transcript and protein levels (Wang et al., 2019; Fig. 1 F, r^2 = 0.89). We next used digital droplet PCR to precisely quantify the abundance of the *Lmna*, *Lmnc*, and *Progerin* transcripts in progeroid mouse tissues and observed that *Progerin* makes up a minor proportion of the transcripts produced from the *Lmna* locus (Fig. 1 G), yet these tissues produce high levels of progerin protein (Fig. 1, C and D). The proportional abundance of *Progerin* transcript and progerin protein are thus very poorly correlated (Fig. 1 H). Taken together, these data indicate that lamin A/C and progerin protein levels are posttranscriptionally modulated in human and mouse tissues. Similarly, poor correlations between transcript and protein levels have been observed for extremely long-lived proteins, such as components of the nuclear pore complex (D'Angelo et al., 2009), leading us to speculate that the A-type lamins are also long-lived proteins.

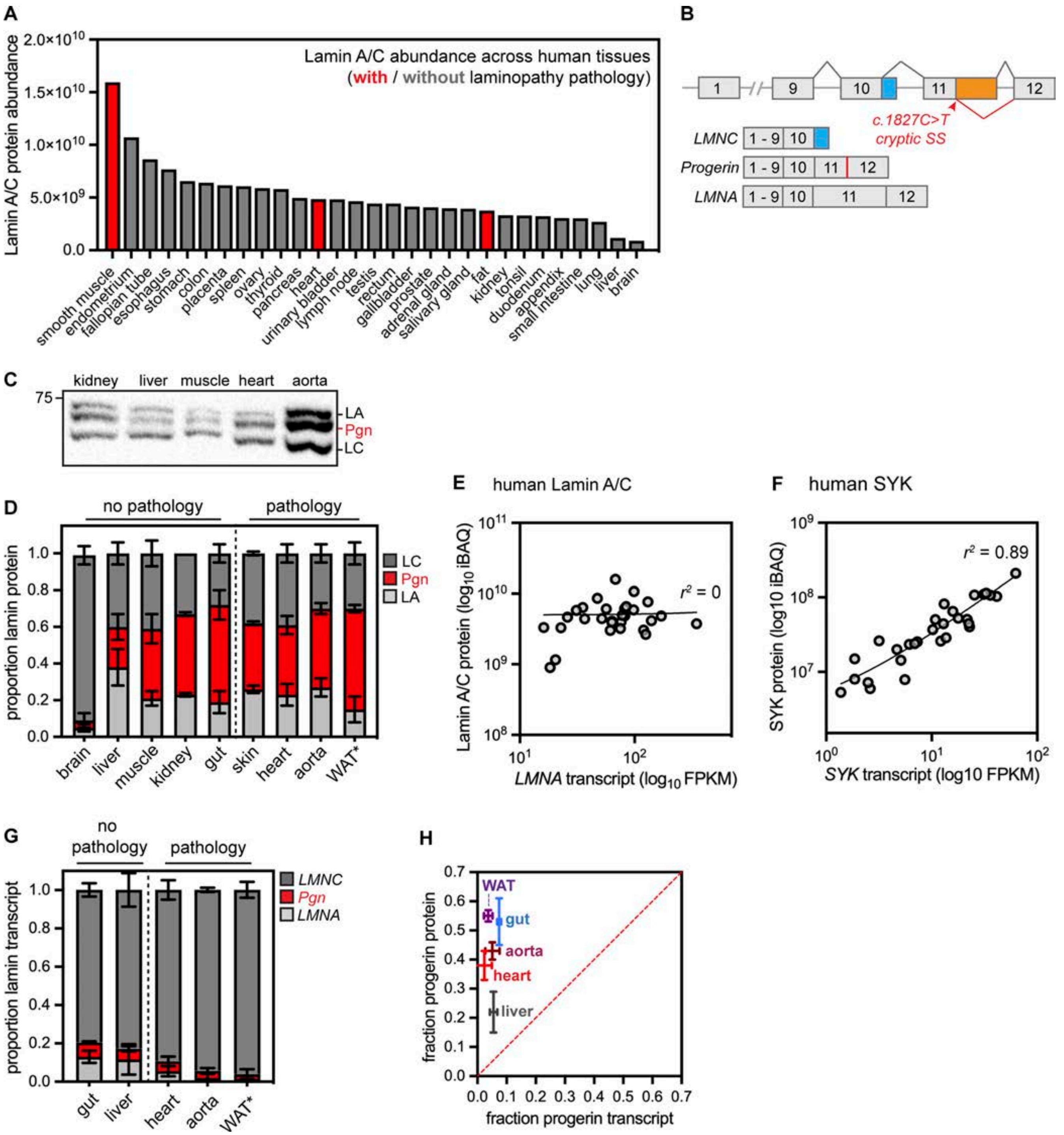

Figure 1. **Poor correlation between transcript and protein abundance for the long-lived disease-linked protein lamin A/C. (A)** iBAQ quantification of lamin A/C absolute protein abundance across 29 human tissues. Data reanalyzed from Wang et al. (2019). **(B)** Diagram of the *LMNA* locus, which produces the *LMNA* (exons 1–12) and *LMNC* (exons 1–10) transcripts. In HGPS, a base pair substitution activates a cryptic splice site, leading to the production of the toxic *progerin* transcript that contains an in-frame deletion in exon 11. **(C)** Representative Western blot of tissue extracts from 9-mo-old $Lmna^{G609G/+}$ mice. 20 µg of protein loaded per lane. **(D)** Quantification of proportional lamin A, lamin C, and progerin protein isoform abundance by Western blotting and densitometry in 9-mo-old $Lmna^{G609G/+}$ mice. * indicates that WAT was analyzed from younger 3-mo-old animals because of the rapidly progressing lipodystrophy in these mice. Sample sizes were as follows: brain (6); liver (6); muscle (4); kidney (2); gut (3); skin (2); heart (6); aorta (2); WAT (5). Error bars, standard deviation. Progerin protein abundance is significantly different across these tissues ($P < 0.0001$ by one-way ANOVA). **(E and F)** Absolute protein abundance (iBAQ) and RNA abundance (RNAseq FPKM) for lamin A/C (E) or SYK (F) across 29 human tissues. Data reanalyzed from Wang et al. (2019). **(G)** Proportional abundance of *Lmna*, *Lmnc*, and *Progerin* transcripts determined by digital droplet PCR in tissues from 9-mo-old $Lmna^{G609G/+}$ mice. * indicates that WAT was analyzed from 3-mo-old animals. Sample sizes were as follows: gut (3); liver (3); heart (3); aorta (2); WAT (3). Error bars, standard deviation. *Progerin* transcript abundance is not significantly different across these tissues ($P > 0.05$ by one-way ANOVA). **(H)** Proportional abundance of *Progerin* transcript and progerin protein are very poorly correlated across tissues from $Lmna^{G609G/+}$ mice. Error bars, standard deviation. Source data are available for this figure: SourceData F1.

Lamin A/C/progerin are long-lived proteins in the cardiovascular system

To test the hypothesis that the A-type lamins have long lifetimes, we sought to determine the turnover rates of these proteins within the tissues of healthy and progeroid mice. Quantification of protein stability can be achieved in vivo by feeding mice chow containing the stable non-toxic isotope ^{15}N, then tracking the rate of incorporation of ^{15}N-labeled amino acids into the proteome over time by mass spectrometry (McClatchy et al., 2007; Hasper et al., 2023). We recently used ^{15}N metabolic labeling to profile trends in protein turnover across healthy mouse tissues (Hasper et al., 2023) and applied the same six-time point, 32-d labeling time course approach to young adult $Lmna^{G609G/+}$ mice. We quantified protein lifetimes in tissues that exhibit progeroid pathology (the aorta, heart, and white adipose tissue) as well as tissues that are spared from overt disease (the intestine and liver). We defined protein turnover rates (k_t) and half-lives ($t_{1/2}$) for 2,744 proteins in the large intestine, 2,098 proteins in the liver, 1,881 proteins in the aorta, 1,429 proteins in the white adipose tissue, and 1,608 proteins in the heart (Fig. S2, A and B; and Table S1). Similar to our previous analyses in healthy mice, proteins generally turn over more rapidly in the progeroid intestine (median $t_{1/2}$ 1.6 d) and liver (median $t_{1/2}$ 2.7 d) than in the progeroid aorta (median $t_{1/2}$ 3.8 d), heart (median $t_{1/2}$ 7.1 d), or fat (median $t_{1/2}$ 9.2 d). Relative to each tissue's proteome, the lamin A/C/progerin proteins are extremely long-lived with half-lives in the top decile in each tissue (Fig. 2 B).

To understand the factors that influence the absolute lifetimes of the A-type lamins across tissues, we must define a parameter that affects the interpretation of differences in protein lifetimes in vivo: the rate of cell turnover. That is, protein turnover in vivo is shaped both by selective proteolytic degradation and non-selective dilution of proteins during cell turnover. We recently developed turnover and replication analysis by ^{15}N isotope labeling (TRAIL; Hasper et al., 2023) to quantify both protein and cell lifetimes from the same tissues and determine cell turnover-corrected protein degradation rates (Fig. 2 A). We applied TRAIL to determine cell turnover rates (k_{div}) and doubling times within the progeroid intestine, liver, fat, and heart (Fig. S2, C and D; and Table S2). (Cell turnover not determined in aorta due to limited sample). Cell doubling times were similar in progeroid and healthy tissues except for the white adipose tissue, where progeroid cells had a doubling time of ∼55 d while age-matched wild-type cells had a doubling time of ∼78 d. This observation likely reflects an increased turnover of adipocytes due to lipodystrophy in this disease state (Merideth et al., 2008).

By subtracting cell turnover rates (k_{div}) from protein turnover rates (k_t), we extrapolated cell cycle–corrected protein degradation rates (k_{deg}) and half-lives ($t_{1/2\mathrm{corr}}$) for proteins in the progeroid intestine, liver, heart, and fat. As we previously observed in wild-type animals (Hasper et al., 2023), protein turnover rates vary across tissues even after cell cycle correction (Fig. 2, E and F; Fig. S2 F; and Table S1). We infer that the rate of cell division as well as tissue-specific factors such as local metabolism or the activity of the proteostasis machinery shape protein lifetimes across tissues.

We found that the lifetimes of the A-type lamins are longer in tissues that exhibit progeroid pathology (the aorta, heart, and fat) compared with those that are spared from pathology (the liver and intestine) in both wild-type and progeroid animals (Table S1). After correcting for the influence of cell turnover, the differences in A-type lamin turnover rates across these tissues were even more stark (Fig. 2, E and F; cell turnover not determined for aorta due to limited sample; $P < 0.0001$ by one-way ANOVA in each genotype). The distribution of half-lives for proteins detected in both the liver and heart tissue of wild-type (Fig. 2 C) and progeroid (Fig. 2 D) animals illustrates the magnitude of this effect; the A-type lamins are among a small group of outlier proteins that have a dramatically longer lifetime in the heart than in the liver. After cell-cycle correction, the predicted half-life for lamin A/C in the healthy heart and fat is ∼3 wk. The average turnover rate of the lamin A/C/progerin proteins slows to >1 mo in the progeroid heart and fat compared with healthy tissues, raising the possibility that progerin turns over even more slowly than wild-type lamin A/C (Fig. 2 F).

Variable biochemical features of lamin A/C/progerin across tissues

The lamins form head-to-tail filaments that bundle laterally (Ben-Harush et al., 2009) and stiffen (Sapra et al., 2020) or undergo structural changes (Swift et al., 2013) in response to mechanical force. Because the heart is a contractile tissue under high strain, we hypothesized that differences in the folding and/or assembly state of the lamin proteins in the heart might underlie the proteins' longer lifetime in this tissue. To test this hypothesis, we subjected tissue homogenates to sequential extractions of increasing stringency—using salt, detergent, and denaturants (Nmezi et al., 2019)—and compared the extent of lamin A/C/progerin extraction after each step. These analyses indicated that the A-type lamins are poorly extractable in heart tissue, where complete extraction was possible only in strongly denaturing conditions (4 M urea; Fig. 3, A–C). In the liver, in contrast, the A-type lamins were efficiently extracted by treatment with high salt (Fig. 3, D–F). These observations imply physicochemical differences in lamin polymers that correlate with the differences in protein turnover rate between these tissues.

Progerin exhibits impaired turnover and accumulates in the cardiovascular system

Lamin A is synthesized as a preprotein that is farnesylated at its C-terminus and then proteolytically cleaved to generate mature lamin A (Burke and Stewart, 2013). The HGPS mutation deletes the protease cleavage site (Eriksson et al., 2003), causing progerin to be constitutively farnesylated. This hydrophobic modification could make progerin more aggregation-prone and/or more recalcitrant to turnover than wild-type lamin A. However, we could not determine whether these closely related isoforms exhibit distinct turnover rates by shotgun proteomics (Fig. 2), as the small subset of peptides that distinguish them from each other were not detected.

To determine whether the HGPS mutation extends protein lifetime, we immunoprecipitated the A-type lamins

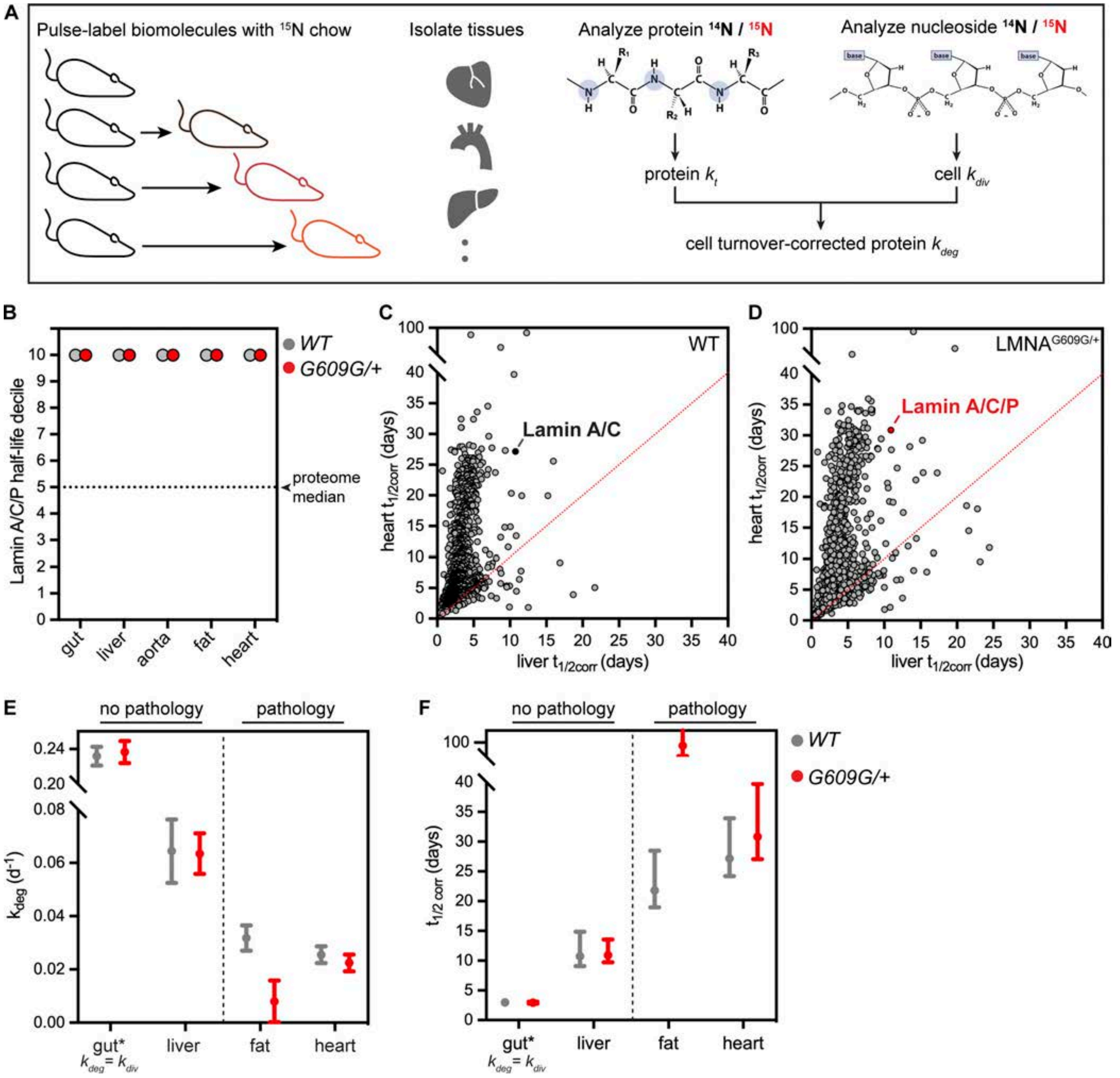

Figure 2. **Quantification of lamin A/C/progerin lifetimes in vivo using TRAIL. (A)** Diagram of turnover and replication by ^{15}N isotope labeling (TRAIL) method for determining protein turnover (k_t) and cell turnover (k_{div}) by tracking ^{15}N incorporation into newly synthesized protein and genomic DNA, respectively. These two parameters are used to determine average bulk cell cycle–corrected protein degradation rates (k_{deg}). Animals were labeled in triplicate for 0, 2, 4, 8, 16, or 32 d before analysis. **(B)** Lamin A/C (gray) and lamin A/C/progerin (red) protein half-lives are in the top 10%/10th decile of half-lives determined in each tissue. **(C and D)** Distribution of half-lives for proteins detected in both the liver and heart of healthy (C) and $Lmna^{G609G/+}$ (D) mice. The A-type lamin proteins (red) are among a group of outliers with a dramatically longer lifetime in the heart than in the liver. **(E and F)** Cell cycle–corrected protein degradation rates (k_{deg}) (E) and half-lives ($t_{1/2corr}$) (F) for A-type lamin proteins in tissues of healthy (gray) and $Lmna^{G609G/+}$ (red) mice. Lamin A/C protein turnover rates are significantly different across tissues of wild-type mice and of $Lmna^{G609G/+}$ mice ($P < 0.0001$ by one-way ANOVA in each genotype) but average turnover rates of lamin A/C/progerin are not significantly different between genotypes in any tissue ($P > 0.05$ by *t* test). *denotes that A-type lamin turnover is equivalent to cell turnover rate in the gut. All data shown are from three independent biological replicate time courses of WT and $Lmna^{G609G/+}$ mice. Error bars, standard error of the mean.

from metabolically labeled progeroid heart, aorta, and liver and performed parallel reaction monitoring mass spectrometry (PRM-MS; Peterson et al., 2012) to quantify peptides unique to lamin A versus progerin (Fig. 4, A and B; and Table S3). We did not monitor lamin-C-only peptides, as lamin C is distinguishable from lamin A only at its C-terminal six amino acids, and this region does not generate any quantifiable and unique tryptic peptides. For maximum sensitivity, we analyzed the

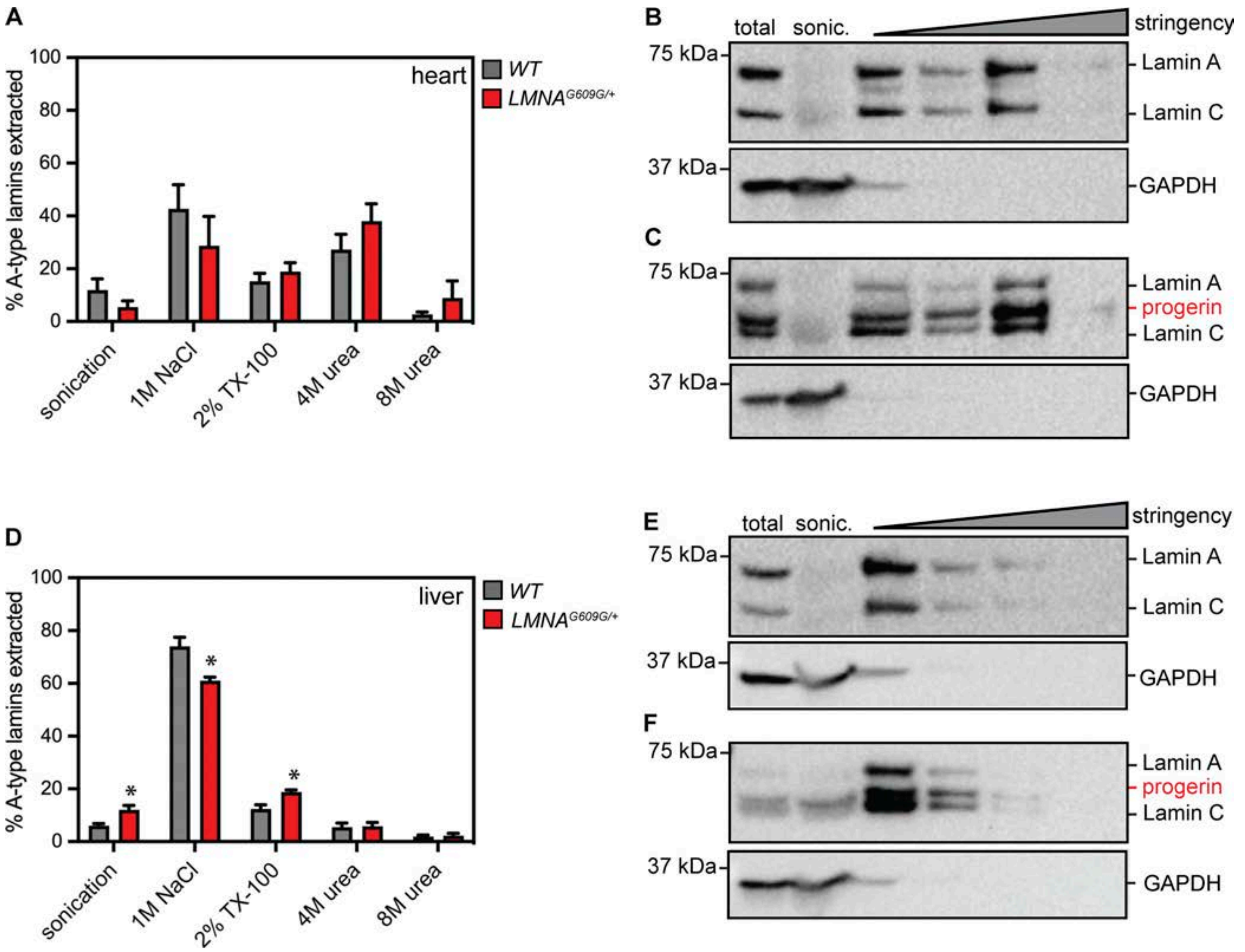

Figure 3. **Variable solubility of lamin A/C/progerin across tissues. (A–F)** Serial extraction of lamin A/C/progerin proteins from the heart (A–C) or liver (D–F) tissue of 4-mo-old healthy (B and E) and *Lmna*$^{G609G/+}$ (C and F) mice. GAPDH indicates effective lysis and release of cytosol in each tissue. While lamin A/C/progerin are readily extractable with high salt in the liver (D–F), strong denaturants are required to completely extract these proteins from the heart (A–C). *indicates significant differences in protein solubility between wild type and *Lmna*$^{G609G/+}$ liver tissue ($P < 0.05$ by unpaired *t* test between genotypes). A and C show analysis of data from three independent biological replicates in WT and *Lmna*$^{G609G/+}$ mice. Error bars, standard error of the mean. Source data are available for this figure: SourceData F3.

labeling time point closest to the half-life of these proteins in each tissue (heart, 32 d; aorta, 16 d; and liver, 8 d). By quantifying the $^{15}N/^{14}N$ isotope abundance ratio for individual peptides unique to each isoform, we compared the relative extent of turnover. These analyses revealed that progerin turns over significantly more slowly than wild-type lamin A in the heart (Fig. 4, C–E) and aorta (Fig. 4, F–H) but not in the liver (Fig. 4, I–K). Comparing these isoform-resolved data to our bulk A-type lamin turnover data leads us to estimate that progerin's lifetime within the cardiovascular system is of the order of months. Altogether, these protein turnover analyses indicate that both tissue context and disease mutations modulate the lifetime of the A-type lamins.

If progerin turnover is impaired compared with wild-type lamin A, one might predict that progerin would accumulate over time. We used tandem mass tagging (TMT) and proteomics (McAlister et al., 2012) to quantify relative protein abundance in healthy versus progeroid tissues from young adult mice (3 mo old) and from animals nearing the end of the HGPS mouse lifespan (9 mo old). These data indicated that the total dose of A-type lamin proteins is significantly increased in the progeroid heart, but not the liver. While the dose of these proteins trends upward in the diseased aorta, this trend is not significant due to variability across samples (Fig. 4 L). Because this analysis cannot distinguish progerin from lamin A/C, these data could indicate either that progerin accumulates over time or that progerin also interferes with the turnover of lamin A/C, leading to the accumulation of all isoforms in the diseased heart.

Progerin expression is associated with impaired proteostasis

Our data indicate that the progerin disease variant accumulates selectively within the cardiovascular system over time. We also observed global changes in protein stability that suggest that proteostasis is broadly disrupted in progeroid tissues (Fig. 5 A).

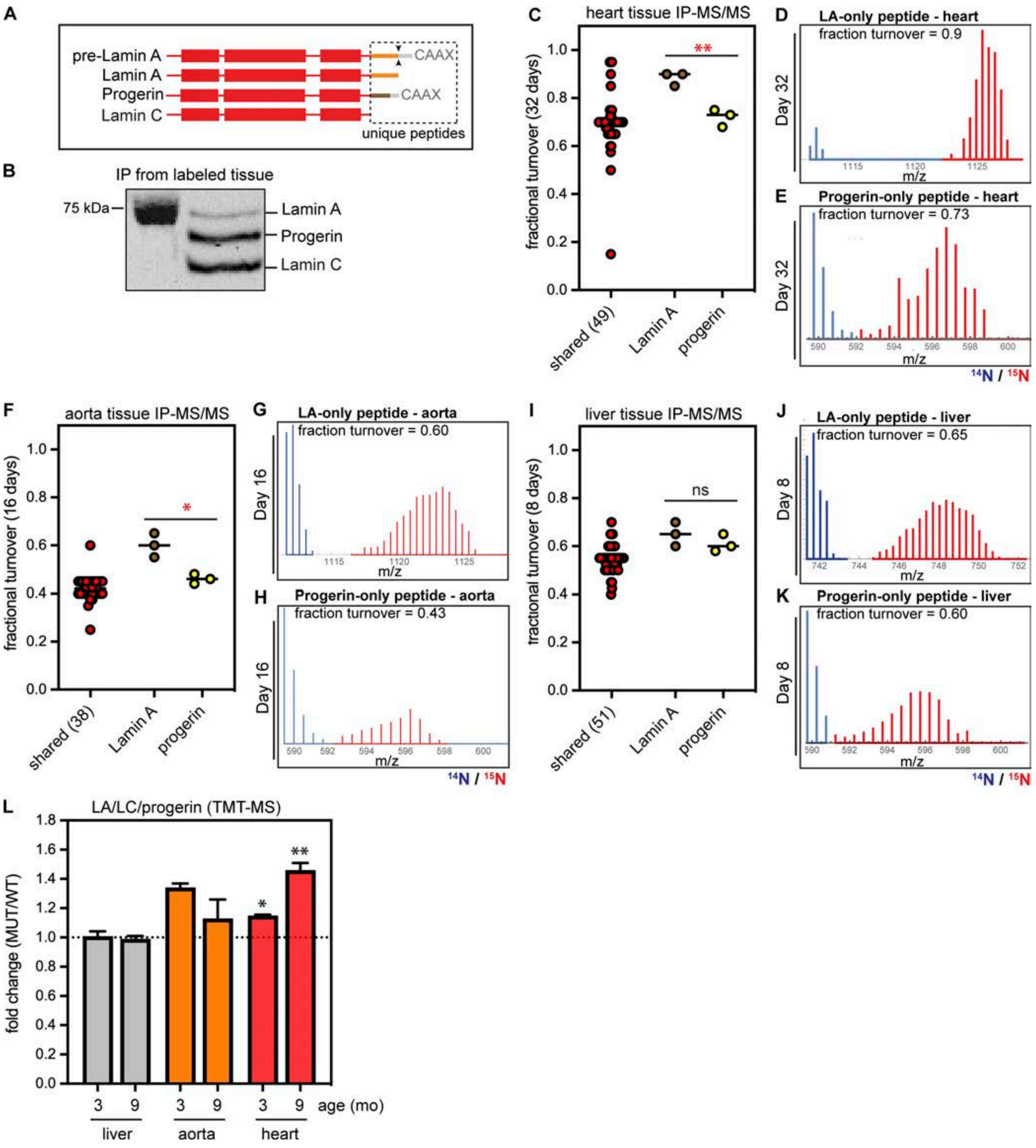

Figure 4. **Isoform-resolved comparison of lamin A versus progerin protein turnover. (A)** Diagram of shared versus unique regions of the pre-lamin A, lamin A, progerin, and lamin C protein isoforms. Dashed box, the region containing unique peptides. **(B)** Representative immunoprecipitation of lamin A/C/progerin from ^{15}N-labeled mouse tissue. **(C)** PRM-MS detection of a lamin A-specific peptide (brown), progerin-specific peptide (yellow), and shared peptides (red) in three biological replicates of heart tissue after 32 d of ^{15}N labeling. Average values plotted for shared peptides (red); individual replicate values plotted for isoform-specific peptides. ** indicates that label incorporation is significantly lower in progerin than lamin A, indicating slower turnover. ($P < 0.01$ by unpaired *t* test). **(D and E)** Representative spectra of lamin A-specific peptide (D) and progerin-specific peptide (E) in the heart. “Old” ^{14}N-labeled peptide is shown in blue and “new” ^{15}N-labeled peptide is shown in red. **(F–K)** PRM detection of lamin A and progerin-specific peptides in three biological replicates of aorta (F–H) and liver (I–K). Progerin turns over more slowly in the aorta (*, $P < 0.05$ by unpaired *t* test) but not in the liver (ns, $P > 0.05$ by unpaired *t* test). **(L)** Analysis of relative protein abundance of $Lmna^{G609G/+}$ versus wild-type mouse tissues at 3 mo ($n = 3$) and 9 mo ($n = 2$) of age by TMT-MS. Total lamin A/C/progerin abundance increases significantly in the progeroid heart, but not in the progeroid liver. Error bars, standard error of the mean. * indicates $P < 0.05$ and ** indicates $P < 0.01$ by one-sample *t* test (Wilcoxon test). Source data are available for this figure: SourceData F4.

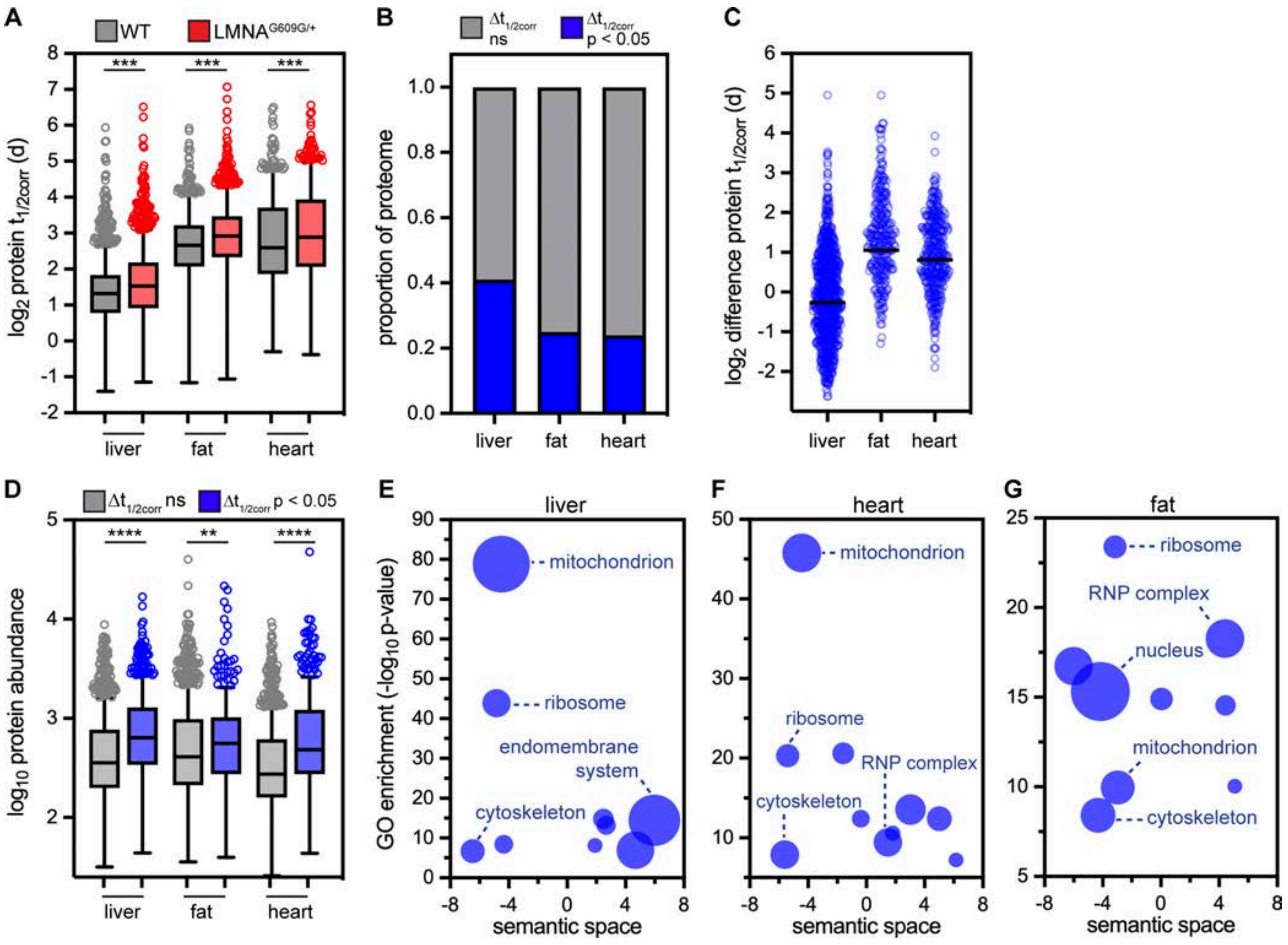

Figure 5. **Effects of progerin on proteome turnover. (A)** Predicted protein half-lives determined for proteins in the liver, fat, and heart muscle of 3-mo-old healthy and *Lmna*$^{G609G/+}$ mice. *** indicates a significant decrease in protein turnover flux in progeroid tissues ($P < 0.0001$ by Mann–Whitney test). Data from wild-type animals reproduced from Hasper et al. (2023). Box (Tukey) plot center line indicates median; box limits indicate 25th to 75th percentiles; whiskers indicate 1.5× interquartile range; points indicate outlier values. **(B)** Proportion of protein in each tissue with significantly different turnover rates in progeroid animals versus wild-type animals (*t* test). **(C)** Difference in protein lifetime (MUT-WT) for proteins with significantly different lifetimes in progeroid animals versus wild-type animals. Liver median difference = +0.8 d ($n = 841$); fat median difference +2.1 d ($n = 349$); heart median difference +1.75 d ($n = 373$). **(D)** Comparison of wild-type protein abundance between proteins with significantly altered lifetime in progeroid tissue (blue) versus proteins with unchanged lifetime in progeroid tissue (gray). Tukey plot. **** indicates that proteins with impaired turnover in progeroid tissue are more abundant in wild-type tissue than proteins with unchanged turnover. (**, $P < 0.01$; ****, $P < 0.0001$ by Mann–Whitney test). **(E–G)** Subsets of Gene Ontology (GO) terms (cellular component) over-represented in proteins with significantly slower turnover in progeroid tissues compared with healthy tissues. Redundant GO terms were removed and non-redundant GO terms organized based on semantic similarity with REViGO. Bubble size corresponds to a number of proteins associated with the GO term, ranging in size from 12 to 175 (E), 14 to 95 (F), and 10 to 157 (G). All data shown are from three independent biological replicate time courses in WT and *Lmna*$^{G609G/+}$ mice.

At an individual protein level, 24–40% of quantified proteins have significantly extended lifetimes in progeroid tissues compared with healthy tissues (Fig. 5 B). The magnitude of this effect is most pronounced in the heart and adipose tissue, where this subset of proteins experiences a median lifetime extension of nearly 2 d compared with age-matched wild-type animals (Fig. 5 C). These proteins are constituents of various structures including mitochondria, ribosomes, the nucleus, and the cytoskeleton (Fig. 5, E–G). As these proteins are components of diverse structures, we hypothesized that shared physicochemical features, not protein localization, might underlie their sensitivity to progerin. Indeed, progerin-sensitive proteins are much more abundant and highly expressed than progerin-insensitive proteins (Fig. 5 D and Fig. S2 G). Altogether, the ability of progerin to impair the turnover of abundant proteins associated with a variety of cellular structures could be consistent with an aggregation-based mechanism of toxicity, as highly abundant proteins are more vulnerable to aggregation (Ciryam et al., 2013; Olzscha et al., 2011).

In this study, we applied quantitative proteomics to explore the origins of tissue specificity in laminopathy syndromes, which are caused by mutations to the abundant and broadly expressed lamin A/C protein. We determined that in relative terms, lamin A/C/progerin are long-lived proteins in all tissues, with a half-life in the top 10% of all proteins quantified in our datasets in each tissue (Fig. 2 B). In absolute terms, the lamin

A/C/progerin proteins have significantly longer lifetimes within the cardiovascular system and fat, which are disrupted in laminopathies, and shorter lifetimes in other tissues such as the liver and intestine. We demonstrated that the A-type lamins are more densely bundled and less extractable in the heart than in the liver. Since substrate unfolding is the major rate-limiting step in protein degradation (Bard et al., 2019), more densely bundled lamin polymers may be more recalcitrant to protein turnover than the same proteins in a less densely bundled state. It will be important to test this hypothesis directly in future experiments.

Our findings suggest that HGPS and other laminopathies may arise as a consequence of disrupted proteostasis. In tissues where the lamins are extremely long-lived, protein synthesis and degradation will happen extremely rarely, perhaps allowing these proteins to undergo molecular "aging" and accumulate damage, misfold, or irreversibly aggregate over time. In fact, lamin A/C is prone to aggregation in the heart of the aged killifish, a short-lived vertebrate model of aging (Chen et al., 2022, *Preprint*). Laminopathy-linked mutations may increase the propensity for misfolding and/or aggregation over time, leading to tissue-specific and time-dependent accumulation of dysfunction. We found that the turnover of the HGPS-causative progerin mutant is selectively impaired within the cardiovascular system, leading to its accumulation over time (Fig. 4). Misfolding and/or aggregation may be shared features of laminopathy mutations (Anderson et al., 2021), raising the question of whether these mutations also impair lamin protein turnover. By analogy to neurodegenerative diseases caused by protein aggregation (Bence et al., 2001), progerin aggregates could exert broad and pleiotropic influence on protein quality control by inducing co-aggregation of other proteins (Kubben et al., 2016) and/or by acting as a sink for the proteostasis machinery. Indeed, hundreds of abundant proteins exhibit impaired turnover in progeroid tissues (Fig. 5), including constituents of mitochondria, ribosomes, the nucleus, and the cytoskeleton. Dysfunction related to each of these cellular structures has been reported in HGPS (Rivera-Torres et al., 2013; Buchwalter and Hetzer, 2017; Scaffidi and Misteli, 2006; Cao et al., 2007). Decreased proteasome activity has been reported in HGPS patient fibroblasts (Gabriel et al., 2015), raising the possibility that decreased flux through the proteasome could contribute to the extension of protein lifetimes that we observe. Recent work indicates that the unfolded protein response and endoplasmic reticulum (ER) stress signaling pathways are activated in the progeroid vasculature and heart (Hamczyk et al., 2019; Vidak et al., 2023), but less so in the liver (Vidak et al., 2023), suggesting that proteostasis may be most impaired in disease-afflicted tissues.

Implications of long lamin protein lifetime for laminopathy therapies

All gene therapies rely on the assumption that targeting a gene will lead to changes to the encoded protein. We have demonstrated that progerin is a long-lived and toxic mutant protein. Because long-lived proteins are rarely synthesized and degraded, they are relatively insensitive to changes in their synthesis rate (D'Angelo et al., 2009). This explains why some gene therapies appear to have significant latency and limited potency in targeting progerin in the cardiovascular system (Puttaraju et al., 2021). The timing and nature of intervention may influence efficacy; progerin clearance may be more effectively achieved with earlier intervention and may be most responsive to irreversible correction of its encoding allele by CRISPR base editing (Koblan et al., 2021). While long lamin A/C protein's lifetime may present a major barrier to treatment in laminopathy syndromes, orthogonal approaches for interfering with mutant protein production or accelerating protein degradation may augment therapy for these devastating diseases (Puttaraju et al., 2021).

Materials and methods

Mouse model

All animal experiments were performed in compliance with relevant ethical regulations and with approval by the Institutional Animal Care and Use Committee at UCSF (IACUC protocol number AN178187, PI: A.B.).

Protein extraction from mouse tissues for Western blotting

Relative abundance of the lamin A, lamin C, and progerin protein isoforms was analyzed in tissues isolated from 9-mo-old *Lmna*$^{G609G/+}$ mice, with the exception of the white adipose tissue (WAT), which was isolated from 3-mo-old mice, because this tissue rapidly diminishes in size due to lipodystrophy in this genotype. Multiple independent biological replicates were analyzed for each tissue: brain (six mice), liver (six mice), muscle (four mice), kidney (two mice), gut (three mice), skin (two mice), heart (six mice), aorta (two mice), and WAT (five mice). Approximately 30 mg of frozen tissue was excised on dry ice with a clean razorblade and placed in a fresh tube. 100 µl of urea lysis buffer (ULB: 8 M urea, 75 mM NaCl, 50 mM HEPES pH 7.9, protease and phosphatase inhibitors) was added to the tube and the tissue was then minced on ice with scissors. ULB was added to a final volume of 600 µl, and the sample was transferred to a Dounce homogenizer. The sample was homogenized for ~40 strokes with the tight pestle and then transferred to a clean microcentrifuge tube. The sample was then probe-sonicated at 4°C (10% amplitude, 10 s, 2 cycles) before being centrifuged (21,000 × *g*, 11 min, 4°C). The supernatant was transferred to a clean tube. Protein concentration was quantified by microBSA assay (Pierce). Lysates were mixed with SDS-PAGE sample buffer, heated to 95°C for 5 min, and cooled. 20 µg of protein were loaded per well for Western blot analysis and proteins were detected with an HRP-conjugated mouse monoclonal antibody that recognizes an N-terminal epitope shared in lamin A, lamin C, and progerin (sc-376248; Santa Cruz). Blots were visualized on a Chemi-Doc (Bio-Rad) and proportional abundance of each protein isoform was determined by densitometry.

Serial extractions of protein from mouse tissues

The relative solubility of the lamin proteins was assayed using a serial extraction protocol adapted from (Nmezi et al., 2019). Experiments were performed on three independent biological replicate samples of heart and liver from 4-mo-old WT and

LMNA$^{G609G/+}$ mice. Approximately 20 mg of frozen tissue was excised on dry ice with a clean razorblade and placed in a fresh tube. Buffer 1 (10 mM HEPES pH 7.4, 2 mM $MgCl_2$, 25 mM KCl, 250 mM sucrose, 1 mM DTT, protease and phosphatase inhibitors; 300 µl) was added to the tube and the tissue was minced on ice. The sample was transferred to a Dounce homogenizer and homogenized for ~40 strokes with the tight pestle and then transferred to a clean microcentrifuge tube. The sample was probe sonicated at 4°C (10% amplitude, 5 s, 2 cycles) and a 50-µl aliquot (whole tissue lysate) was retained. The remaining sample was then centrifuged (20,000 × *g*, 5 min, 4°C). The supernatant (S1) was retained. The pellet was resuspended in Buffer 2 (20 mM HEPES pH 7.4, 1 M NaCl, protease and phosphatase inhibitors; 250 µl) and incubated for 20 min at RT with end-over-end rotation. The sample was then centrifuged (20,000 × *g*, 5 min; RT) and the supernatant (S2) was retained. The pellet was resuspended in Buffer 3 (20 mM HEPES pH 7.4, 1 M NaCl, 2% Triton-X-100, protease, and phosphatase inhibitors; 250 µl) and incubation and centrifugation were repeated. The supernatant (S3) was retained, and the pellet was resuspended in Buffer 4 (20 mM HEPES pH 7.4, 1 M NaCl, 4 M urea, protease, and phosphatase inhibitors; 250 µl) and incubation and centrifugation were repeated. Finally, the supernatant (S4) was retained, and the pellet was resuspended in Buffer 5 (20 mM HEPES pH 7.4, 1 M NaCl, 8 M urea, protease, and phosphatase inhibitors; 250 µl) and incubation and centrifugation were repeated. The final supernatant (S5) was retained. An aliquot of the tissue lysate and equal proportions of each supernatant were loaded on SDS-PAGE gels and processed for Western blotting with an HRP-conjugated mouse monoclonal antibody that recognizes an N-terminal epitope shared in lamin A, lamin C, and progerin (sc-376248; Santa Cruz).

RNA extraction from mouse tissues

The relative abundance of the lamin A, lamin C, and progerin transcript isoforms was analyzed in tissues isolated from 9-mo-old *Lmna*$^{G609G/+}$ mice, with the exception of the WAT, which was isolated from 3-mo-old mice, because this tissue rapidly diminishes in size due to lipodystrophy in this genotype. Three independent biological replicate mice were analyzed for the gut, liver, heart, and WAT; aortas from two independent biological replicate mice were analyzed. Approximately 30 mg of frozen tissue was excised on dry ice with a clean razorblade and placed in a fresh microcentrifuge tube. 100 µl of TRIzol was added and the tissue was minced with scissors on ice. Additional TRIzol was added to a final volume of 500 µl and the sample was transferred to a Dounce homogenizer. The sample was homogenized for ~40 strokes with the tight pestle and then transferred to a clean microcentrifuge tube. The sample was incubated for 5 min at RT before chloroform (100 µl) was added. The sample was mixed by inversion and incubated for 3 min and then centrifuged (12,000 × *g*, 15 min, 4°C). The aqueous RNA-containing supernatant was carefully removed and pipetted into a fresh tube. 1 µl of GlycoBlue and 250 µl isopropanol were added to the supernatant, incubated for 10 min at RT, and then centrifuged (12,000 × *g*, 10 min, 4°C). The supernatant was removed from the blue RNA–glycogen pellet and then the pellet was resuspended in 500 µl 75% ethanol and centrifuged (7,500 × *g*, 5 min, 4°C). The supernatant was removed, and the pellet was allowed to air dry for 5–10 min. The pellet was resuspended in 50 µl nuclease-free water (Ambion) and RNA concentration was determined by NanoDrop.

Transcript quantification with digital droplet PCR

For each sample, 1 µg of RNA was diluted into 15 µl reverse transcription reactions using the iScript RT kit (Bio-Rad) and reactions were carried out following the manufacturer's instructions. Each cDNA reaction was diluted to 10 ng/µl (RNA equivalents). For each sample, 20 ng (RNA equivalents) was combined with 10 µl of 2× ddPCR Supermix for Probes (no UTP; Bio-Rad), 1 µl of a 20× FAM primer/probe set, 1 µl of a HEX primer/probe set, and nuclease-free water to a final volume of 20 µl. *Lmna* primers and probe sequences are listed below and are adapted from Puttaraju et al. (2021). *mTfrc* primers and probe sequence were from Bio-Rad (PrimerPCR ddPCR Expression Probe Assay for Tfrc Mouse [HEX]). Reaction droplets were generated on a Droplet Maker (Bio-Rad), ddPCR reactions were run on a C1000 Thermocycler (Bio-Rad), and reactions were analyzed on a QX100 ddPCR reader (Bio-Rad) according to the manufacturer's instructions.

ddPCR allows the absolute quantification of transcript abundance based on the ratio of positive to negative droplets and is unaffected by primer-specific variables such as reaction efficiency (Hindson et al., 2011). We used absolute ddPCR quantification to determine the abundance of the *Lmna*, *Lmnc*, and *Progerin* transcripts (copies per droplet). *mTfrc* reactions were run in the HEX channel of each ddPCR reaction as a positive control but were not used to normalize *Lmna* transcript measurements. Transcript abundance was expressed as a proportion for each transcript. For example, for *Lmna*:

$$\text{proportional abundance } Lmna = [Lmna]/([Lmna] + [Lmnc] + [Progerin])$$

ddPCR probe and primer sets for mouse Lmna, Lmnc, and Progerin were as previously described (Puttaraju et al., 2021) and as listed in the following Table 1.

Metabolic labeling of mice and tissue isolation

As recently described (Hasper et al., 2023), we performed a six-time point, 32-d ^{15}N labeling time course (0, 2, 4, 8, 16, and 32 d of labeling) with a total of three animals of both sexes per labeled time point and two animals for the day 0 (unlabeled) time point (see Fig. S3). Time courses were performed in *Lmna*$^{G609G/+}$ C57Bl/6 mice at ~9 wk of age. These time courses were performed in parallel to age-matched wild-type mouse labeling time courses that were recently published (Hasper et al., 2023) and are the source of the wild-type data shown in this study. ^{14}N and ^{15}N mouse chow was obtained from Silantes. Animals were first habituated to the chow formulation by feeding ^{14}N (normisotopic) food for 1 wk; animals were then transitioned to ^{15}N chow throughout the labeling period (roughly 3 g/animal/d). Animals were sacrificed by CO_2 inhalation followed by cervical dislocation, followed by tissue dissection and flash-freezing by submersion in liquid nitrogen.

Table 1. **ddPCR probe and primer sets for mouse *Lmna*, *Lmnc*, and *Progerin* were as previously described (Puttaraju et al., 2021) and as listed in the following table**

Target	Primer (F)	Primer (R)	Probe
Lamin A (FAM)	5′-ACCGCTCTCATCAACTCCAC-3′	5′-GCGGCGGCTGCCACTCAC-3′	5′-GGTTGAGGACAATGAGGATG-3′
Progerin (FAM)	5′-AGAAGAGCTCCTCCATCACC-3′	5′-ACATGATGCTGCAGTTCTGG-3′	5′-TGGAGCGGGAGCCCAGAGCTC-3′
Lamin C (FAM)	5′-ATCCATCTCCTCTGGCTCTT-3′	5′-ACATGATGCTGCAGTTCTGG-3′	5′-TCCAGTCCCCGGAGCCAG/AGCT-3′

Protein extraction and sample preparation for LC-MS/MS

Protein extraction

Approximately 30 mg of frozen tissue was excised on dry ice with a clean razorblade and placed in a fresh tube. 100 µl of protein extraction buffer (PEB: 5% SDS, 100 mM TEAB, protease, and phosphatase inhibitors, pH ∼7) was added to the tube. The tissue was minced on ice; PEB was added to bring the final volume to 600 µl and then the sample was transferred to a Dounce homogenizer. The sample was homogenized for ∼40 strokes with the tight pestle and then transferred to a clean microcentrifuge tube. The sample was then probe-sonicated at 4°C (10% amplitude, 10 s, 2 cycles) before being centrifuged (21,000 × *g*, 11 min, 4°C). The supernatant was transferred to a clean tube and aliquots were separated for proteomics and protein quantification by microBSA assay (Pierce).

Trypsinization

Samples were diluted to 1 mg/ml in 5% SDS and 100 mM TEAB, and 25 µg of protein from each sample was reduced with dithiothreitol to 2 mM, followed by incubation at 55°C for 60 min. Iodoacetamide was added to 10 mM and incubated in the dark at room temperature for 30 min to alkylate proteins. Phosphoric acid was added to 1.2%, followed by six vol of 90% methanol and 100 mM TEAB. The resulting solution was added to S-Trap micros (Protifi) and centrifuged at 4,000 × *g* for 1 min. The S-Traps containing trapped protein were washed twice by centrifuging with 90% methanol and 100 mM TEAB. 1 µg of trypsin was brought up in 20 µl of 100 mM TEAB and added to the S-Trap, followed by an additional 20 µl of TEAB to ensure the sample did not dry out. The cap to the S-Trap was loosely screwed on but not tightened to ensure the solution was not pushed out of the S-Trap during digestion. Samples were placed in a humidity chamber at 37°C overnight. The next morning, the S-Trap was centrifuged at 4,000 × *g* for 1 min to collect the digested peptides. Sequential additions of 0.1% TFA in acetonitrile and 0.1% TFA in 50% acetonitrile were added to the S-trap, centrifuged, and pooled. Samples were frozen and dried down in a Speed Vac (Labconco) prior to TMTpro labeling.

TMT labeling

Samples were reconstituted in TEAB to 1 mg/ml and then labeled with TMTpro 16plex reagents (Thermo Fisher Scientific) following the manufacturers' protocol. Briefly, TMTpro tags were removed from the −20°C freezer and allowed to come to room temperature, after which acetonitrile was added. Individual TMT tags were added to respective samples and incubated at room temperature for 1 h 5% hydroxylamine was added to quench the reaction, after which the samples for each experiment were combined into a single tube. Since we performed abundance quantitation on unlabeled peptides, 0-d samples were added to four of the unused channels, increasing the signal for the unlabeled peptides. TMTpro tagged samples were frozen, dried down in the Speed Vac, and then desalted using homemade C18 spin columns to remove excess tags prior to high pH fractionation.

High pH fractionation

Homemade C18 spin columns were activated with two 50 µl washes of acetonitrile via centrifugation, followed by equilibration with two 50-µl washes of 0.1% TFA. Desalted, TMTpro tagged peptides were brought up in 50 µl of 0.1% TFA and added to the spin column. After centrifugation, the column was washed once with water and then once with 10 mM ammonium hydroxide. Fractions were eluted off the column with centrifugation by stepwise addition of 10 mM ammonium hydroxide with the following concentrations of acetonitrile: 2%, 3.5%, 5%, 6.5%, 8%, 9.5%, 11%, 12.5%, 14%, 15.5%, 17%, 18.5%, 20%, 21.5%, 27%, and 50%. The 16 fractions were concatenated down to 8 by combining fractions 1 and 9, 2 and 10, 3 and 11, etc. Fractionated samples were frozen, dried down in the Speed Vac, and brought up in 0.1% TFA prior to mass spectrometry analysis.

LC-MS/MS analysis

Data collection

Peptides from each fraction were injected onto a homemade 30-cm C18 column with 1.8 µm beads (Sepax), with an Easy nLC-1200 HPLC (Thermo Fisher Scientific), connected to a Fusion Lumos Tribrid mass spectrometer (Thermo Fisher Scientific). Solvent A was 0.1% formic acid in water, while solvent B was 0.1% formic acid in 80% acetonitrile. Ions were introduced to the mass spectrometer using a Nanospray Flex source operating at 2 kV. The gradient began at 3% B and was held for 2 min, increased to 10% B over 7 min, increased to 38% B over 94 min, then ramped up to 90% B in 5 min, and held for 3 min, before returning to starting conditions in 2 min and re-equilibrating for 7 min, for a total run time of 120 min. The Fusion Lumos was operated in a data-dependent mode, employing the MultiNotch Synchronized Precursor Selection MS3 method to increase quantitative accuracy (McAlister et al., 2014). The cycle time was set to 3 s. Monoisotopic Precursor Selection (MIPS) was set to peptide. The full scan was done over a range of 400–1,500 m/z, with a resolution of 120,000 at m/z of 200, an AGC target of 4e5, and a maximum injection time of 50 ms. Peptides with a charge state between 2 and 5 were picked for fragmentation. Precursor ions were fragmented by collision-induced dissociation (CID) using a collision energy of 35% and an isolation width of 1.0 m/z. MS2 scans were collected in the ion trap with an AGC target of 1e4 and a maximum injection time of 35 ms. MS3 scans were performed by fragmenting the 10 most intense fragment ions between 400 and 2,000 m/z, excluding ions that were 40 m/z less and 10 m/z greater than the precursor peptide, and using higher energy collisional dissociation (HCD). MS3 ions were detected in the Orbitrap with a resolution of 50,000 at m/z 200 over a scan range of 100–300 m/z. The isolation width was set to 2 Da, the collision energy was 60%, the AGC was set to 1e5, and the maximum injection time was set to 100 ms. Dynamic exclusion was set to 45 s.

Data analysis

Raw data was searched using the SEQUEST search engine within the Proteome Discoverer software platform, version 2.4 (Thermo Fisher Scientific), using the Uniprot mouse database (downloaded January 2020). Trypsin was selected as the enzyme allowing up to two missed cleavages, with an MS1 mass tolerance of 10 ppm and an MS2 mass tolerance of 0.6 Da. Carbamidomethyl on cysteine and TMTpro on lysine and peptide N-terminus were set as fixed modifications, while oxidation of methionine was set as a variable modification. The percolator was used as the FDR calculator, filtering out peptides that had a q-value >0.01. Reporter ions were quantified using the Reporter Ions Quantifier node, with an integration tolerance of 20 ppm, and the integration method was set to “most confident centroid.” Protein abundances were calculated by summing the signal to noise of the reporter ions from each identified peptide while excluding any peptides with an isolation interference >30% or SPS matches <65%.

Kinetic model

The kinetic model applied in this study has been previously described (Welle et al., 2016). Briefly, we are assuming that protein synthesis is a zero-order process, occurs at a constant fractional rate, and that the total protein concentration of each cell does not change during the experimental time course. The dilution of the protein pool due to cell division can be modeled as a first-order exponential process. Thus, the fractional turnover of unlabeled proteins during the labeling time course can be regarded as a first-order kinetic process that can be modeled based on the following exponential equation:

$$\text{fraction unlabeled protein } (t) = e^{-k_t * t} \tag{1}$$

and:

$$k_t = k_{deg} + k_{div}$$

where: k_t is the clearance rate (observed rate of fractional labeling), k_{deg} is the rate of protein degradation, and k_{div} is the rate of cell division.

The determination of k_t values was conducted as previously described (Welle et al., 2016) using the decay of the TMT reporter signals of unlabeled proteins. Protein-level TMT reporter abundances for unlabeled proteins for each replicate experiment were first normalized by dividing by the intensity of the t0 reporter and then the replicate experiments were aggregated in a single kinetic curve. In fitting the exponential decay curves of the unlabeled protein signals, a constant fractional baseline at infinite time was incorporated in the fitting equation. The equation used for fitting the curves was therefore $intensity = baseline + (1 - baseline) * e^{-k_t * time}$. The goodness of fit for least squares fits were assessed by determining the R^2, P value, and *t* statistic of the fits (see Table S1). For subsequent analyses, only protein k_t measurements that were obtained from all three replicate experiments incorporated data from four or more peptide spectral matches (PSMs) and had *t* statistic values >3 were considered.

Nucleic acid extraction and sample preparation for LC-MS/MS

Genomic DNA extraction

Approximately 30 mg of frozen tissue was excised on dry ice with a clean razorblade and placed in a fresh tube. 100 µl of TRIzol reagent (Invitrogen) was added, and the tissue was rapidly minced on ice. An additional 400 µl of TRIzol was added, and the sample was then transferred to a Dounce homogenizer. The tissue was subjected to ∼40 strokes with the tight pestle until smooth and then transferred back to the original tube. The sample was incubated for at least 5 min before the addition of 100 µl chloroform followed by mixing and a further 3 min of incubation. The sample was then centrifuged (12,000 × *g*, 15 min, 4°C) and the upper RNA-containing aqueous layer was discarded. 150 µl of absolute ethanol was added to the remaining sample and then inverted several times to mix. After 3 min of incubation at room temperature, the sample was centrifuged (2,000 × *g*, 5 min, 4°C). The protein-containing supernatant was removed and then the DNA-containing pellet was resuspended in 500 µl of absolute ethanol and incubated for 30 min. The sample was then centrifuged (2,000 × *g*, 5 min, 4°C) and the supernatant was discarded. Sequential washes were then repeated with 95%, 85%, and 75% ethanol, after which the pellet was air-dried for 5–10 min. The pellet was then resuspended in 200 µl nuclease-free water (Ambion) at 56°C and then incubated at 56°C with shaking for 30 min to resuspend the pure DNA. The sample was centrifuged (12,000 × *g*, 10 min, 4°C) and then the supernatant containing pure DNA was moved to a clean tube. DNA concentration was determined with a NanoDrop spectrophotometer.

Digestion of genomic DNA to short oligonucleotides

3–5 µg of pure genomic DNA was diluted to a 50 µl volume in nuclease-free water and then combined with 50 µl of 2× dinucleotide buffer (DB: 5 mU/µl benzonase, 40 mU/µl shrimp alkaline phosphatase, 20 mM Tris pH 7.9, 100 mM NaCl, 20 mM $MgCl_2$). Samples were incubated overnight at 37°C. Spin-X UF Concentrators (Corning) were rinsed with 200 µl buffer (20 mM Tris pH 7.9, 100 mM NaCl, 20 mM $MgCl_2$) and then samples were applied and centrifuged through (12,000 × *g*, 5 min, RT). The eluate was collected for analysis.

Digestion of genomic DNA to mononucleosides

We extracted mononucleosides from genomic DNA similarly to a previously described method (Quinlivan and Gregory, 2008) with some modifications. 1–3 µg of pure genomic DNA was diluted to a 50 µl volume in nuclease-free water and then combined with 50 µl of 2× mononucleoside buffer (MB: 5 mU/µl benzonase, 40 mU/µl shrimp alkaline phosphatase, 60 µU/µl phosphodiesterase I, 20 mM Tris pH 7.9, 100 mM NaCl, and 20 mM $MgCl_2$). Samples were incubated overnight at 37°C. Spin-X UF Concentrators (Corning) were rinsed with 200 µl buffer (20 mM Tris pH 7.9, 100 mM NaCl, and 20 mM $MgCl_2$) and then samples were applied and centrifuged through (12,000 × *g*, 5 min, RT). The eluate was collected for analysis.

Mononucleoside and dinucleotide LC-MS/MS

Mononucleoside analyses were carried out by adapting a previously described method (Su et al., 2014) using a Dionex Ultimate 3000 UHPLC coupled to a Q Exactive Plus mass spectrometer (Thermo Fisher Scientific). After purification, analytes were separated on a Hypersil Gold 2.1 × 150 mm column and protected by a 2.1 × 10 mm Hypersil Gold guard column (Thermo Fisher Scientific). The mobile phases were A: 0.1% formic acid in water and B: 0.1% formic acid in acetonitrile. The flow rate was set to 400 µl/min and the column oven was set to 36°C. 10 µl of each sample was injected and the analytes were eluted using the following gradient: 0 min: 0% B, 6 min: 0% B, 8.5 min: 80% B, 9.5 min: 80% B, 10 min: 0% B, and 13 min: 0% B. The Q Exactive Plus was operated in positive mode with a heated electrospray ionization (HESI) source. The spray voltage was set to 3.5 kV, the sheath gas flow rate was set to 40, and the auxiliary gas flow rate was set to 7, while the capillary temperature was set to 320°C. A parallel reaction monitoring (PRM) method was used to quantify the unlabeled nucleotide along with all of its N15 isotopes in a single scan. This was accomplished by using wide (8 m/z) isolation widths when selecting the nucleotides for fragmentation. By employing this method, we were able to quantify the level of labeling by looking at the intensity of each N15-labeled base in the MS2 scan. Fragment ions were detected in the Orbitrap with a resolution of 70,000 at m/z 200. Using a high-resolution MS2 scan allowed us to resolve N15 and C13 isotopes. Peak areas from the fragment ions were extracted with a 10 ppm mass tolerance using the LC Quan node of the XCalibur software (Thermo Fisher Scientific).

Dinucleotide analyses were carried out using the same instrumentation, column, mobile phases, column temperature, and flow rate employed by the mononucleoside experiments. The gradient was changed to optimize dinucleotide separation as follows: 0 min: 5% B, 0.5 min: 5% B, 2.5 min: 90% B, 3.25 min: 90% B, 3.5 min: 5% B, and 5.5 min: 5% B. The Q Exactive Plus was operated using the same tune settings as the mononucleotide experiment. However, instead of a PRM method, a full scan method from 500 to 650 m/z was developed to quantify the dinucleotides dCdC, TT, dAdA, and dGdG along with their corresponding N15 isotopes. Precursor ions were detected in the Orbitrap with a resolution of 140,000 at m/z 200 using the high-resolution MS1 scan to try to separate N15 and C13 isotopes as much as possible. Peak areas from the fragment ions were extracted with a 10 ppm mass tolerance using the LC Quan node of the XCalibur software (Thermo Fisher Scientific).

Measurement of k_{div}

To accurately measure rates of cell division (k_{div}) while factoring in the effects of incomplete labeling and nucleotide recycling, we considered the time-dependent labeling patterns of mononucleosides derived from genomic DNA. Upon initiation of ^{15}N labeling, newly synthesized DNA strands can incorporate nucleotides from a precursor pool that includes fully ^{15}N-labeled nucleotides derived from the dietary source, partially labeled species (containing one to four ^{15}N atoms) derived by biosynthesis from incompletely labeled ^{15}N precursors, and completely unlabeled nucleotides derived from recycling. Therefore, it may not be possible to accurately determine the ratio of new to old strands (and hence k_{div}) from the mononucleotide data alone. We previously used the labeling pattern of dinucleotides to resolve this ambiguity (Hasper et al., 2023). The isotopologue distribution of labeled (non-monoisotopic) peaks in the dinucleotide spectra is dependent on the composition of the nucleotide precursor pool. Through regression analyses, we determined that within all tissues and time points analyzed in this study, the isotopologue distributions of the dinucleotide data could be best modeled based on the assumption that newly synthesized strands had very low levels of fully unlabeled nucleotides. Hence, the fractional population of labeled non-monoisotopic peaks within dinucleotide and mononucleotide data were consistent with each other and could be used to determine the fractional population of new strands. For each tissue, fractional labeling of mononucleotide and dinucleotides for all four bases were combined and the aggregated dataset was fit to a single exponential equation to determine the first-order rate constant for division (k_{div}). These data appear in Table S2.

Analysis of proteomic data

Quality filtering and analysis of k_t values

Proteomic data was acquired in the form of 16-plex TMT replicates containing two full six-time point time courses (one from wild-type animals and one from progeroid animals). For each genotype within each TMT replicate, proteins were filtered to retain only those detected with at least three peptide spectral matches (PSMs) in all time points. Proteins that met these criteria were then filtered per genotype within each TMT replicate based on goodness of fit using the *t* statistic. The *t* statistic is equal to the turnover rate (k_t) divided by the standard error of that value. This metric determines to what extent measurement error influences k_t. We applied a minimum *t* statistic cutoff of 3, meaning that the magnitude of the turnover rate k_t is at least three times the magnitude of the standard error. Between 50% and 63% of detected proteins passed these coverage and goodness-of-fit criteria. Along with the sample size, the *t* statistic can be used to determine a P value that indicates the probability that the turnover rate reported has a meaningful non-zero value. The k_t, standard error, *t* statistic, and P value for each protein are reported in Table S1. The k_t, standard error, and sample size were used to perform per-protein statistical tests across tissues and to identify proteins with significantly different turnover kinetics between tissues. These data are reported in Table S1.

Determination of relative protein abundance within tissues

To evaluate relative protein abundance between genotypes within tissues of 3-mo-old mice, technical replicate unlabeled wild-type and progeroid samples from each multiplexed TMT run were first channel normalized, then the geometric mean was calculated to determine mean normalized intensities for each biological replicate. Protein abundance was then length-normalized by dividing each protein's normalized intensity by the number of amino acids. Finally, samples were normalized for comparison across biological replicates by normalizing each channel to the maximum value detected. The geometric mean abundance across all biological replicates was calculated by determining the geometric mean of the length- and channel-normalized protein abundance. Finally, the fold change of protein abundances between wild type and progeroid tissues was determined.

Additional multiplexed TMT experiments were performed to compare protein abundances within tissues from 9-mo-old wild-type and progeroid mice. In these experiments, two biological replicate samples were analyzed in technical duplicate for each genotype in an eight-plex TMT experiment per tissue. Raw data were subjected to the same sequence of technical replicate averaging, protein length normalization, channel normalization, biological replicate averaging, and fold-change determination described above.

Protein immunoprecipitation from mouse tissues

Metabolically labeled tissue extracts from the aorta, heart, and liver of three progeroid animals prepared as described above in PEB for proteomic analysis were used for immunoprecipitation as follows. Approximately 1,300–1,500 µg of lysate (100 µl) was aliquoted into a fresh tube and diluted to 2 ml final volume in a dilution buffer (10 mM Tris pH 7.4, 150 mM NaCl, 1% Triton X-100, 1% deoxycholate, 2.5 mM $MgCl_2$, protease, and phosphatase inhibitors). For each sample, 60 µl of Protein G magnetic beads (Life Technologies) was rinsed and resuspended in dilution buffer and then added to the diluted lysate. The sample was incubated at 4°C with rotation for 30 min. Beads were removed and the precleared supernatant was transferred to a clean tube; 5% of the sample was reserved as input. A mixture of two anti-Lamin A/C antibodies was used to immunoprecipitate lamin A, lamin C, and progerin: lamin A/C E-1 (sc-376248, 20 µl per IP; Santa Cruz) and lamin A/C (#39288 Clone 3A6-4C11, 5 µl per IP; Active Motif). The IP was incubated overnight at 4°C with nutation. 60 µl of prerinsed Protein G beads was then added to the sample and incubated for 30 min at 4°C with nutation. Beads were collected on a magnetic stand and supernatant (flow-through) was saved in a fresh tube. Beads were washed in 3 × 1 ml of wash buffer (10 mM Tris pH 7.4, 150 mM NaCl, 0.5 mM EDTA, 0.1% SDS, 1% Triton X-100, 1% deoxycholate, 2.5 mM $MgCl_2$, protease, and phosphatase inhibitors). Following the third wash, the liquid was carefully removed using a gel loading tip; 2× SDS-PAGE sample buffer was added to the beads and proteins were eluted by boiling for 5 min at 95°C.

To check the efficiency of each IP, equal proportions of the input and flow-through fractions were analyzed by Western blotting for lamin A/C (E-1 HRP, sc-376248 HRP; Santa Cruz). If a noticeable decrease in protein abundance was apparent in the flow-through sample, the IP samples were run on an SDS-PAGE gel and stained with colloidal Coomassie stain. A gel slice containing the lamin A, lamin C, and progerin bands was cut out for downstream mass spectrometry analysis.

SIM/PRM-MS of lamin and progerin peptides

Data collection

SIM/PRM was performed as described above with the following changes. The gradient began at 3% B and held for 2 min, increased to 10% B over 5 min, increased to 38% B over 38 min, and then ramped up to 90% B in 3 min and held for 3 min before returning to starting conditions in 2 min and re-equilibrating for 7 min, for a total run time of 60 min. The Fusion Lumos was operated using dual experiments, the first being a tSIM scan and the second being a PRM scan. Each tSIM scan targeted ions with an m/z of 597.7463 using an isolation window of 20 m/z, covering the range of the unique Progerin peptide (AAGGAGAQSSQNC + farnesylation and carboxymethylation) and all possible N15 isotopes. The resolution was set to 120,000 at m/z of 200, an AGC target of 1e5, and a maximum injection time of 246 ms. The PRM scan fragmented precursor ions with an m/z of 589.7463 by collision-induced dissociation (CID) using a 1.6 m/z isolation width. The collision energy was set to 30% with a maximum injection time of 250 ms, and an AGC target of 1e4. The Ion Trap Scan Rate was set to "Rapid."

Data analysis

The presence of progerin was validated using raw MS2 data. Raw SIM data were searched for precursor ions with an m/z of 589.7463 and z of 2 in addition to all possible N15 isotopologues. The intensity of each isotopologue was measured using the Thermo XCalibur Qual Browser.

Online supplemental material

Fig. S1 contains quantitative proteomic data showing estimated lamin A, B1, and B2 isoform copy numbers per cell across human tissues. Fig. S2 shows protein turnover and protein abundance data comparisons for the proteomes of healthy and progeroid mouse tissues. Fig. S3 provides data on animal weights through the course of metabolic labeling. Table S1 contains protein turnover data in wild-type and progeroid mouse tissues. Table S2 reports cell turnover data in wild-type and progeroid mouse tissues. Table S3 contains isotope enrichment measurements for lamin A and progerin peptides in ^{15}N-labeled progeroid mouse tissue.

Data availability

LC-MS/MS data have been deposited in the ProteomeXchange Consortium via the PRIDE partner repository, accessible at https://www.ebi.ac.uk/pride under accession code PXD033649.

Acknowledgments

We thank Yana Blokhina, Biao Wang, Esther Paolo Mirasol, Carlos Lizama Valenzuela, and Xi Chen for assistance with tissue dissections; Bryan Ryder and Jason Gestwicki for discussions on proteostasis; Jonah Cool, Akiko Hata, and David Julius for critical reading of the manuscript; and all members of the Buchwalter lab for encouragement, ideas, and memes throughout the project period.

We acknowledge the Progeria Research Foundation (A. Buchwalter), the Chan Zuckerberg Biohub (A. Buchwalter), and the National Institutes of Health (R35 GM119502 and S10 OD025242, S. Ghaemmaghami) for funding support.

Author contributions: J. Hasper performed in vivo labeling experiments, tissue isolations, protein and DNA extractions, and protein biochemistry experiments with assistance from A. Buchwalter. J. Hryhorenko, K. Welle, and K. Swovick prepared and ran samples for LC-MS/MS. A. Buchwalter, J. Hasper, K. Welle, K. Swovick, and S. Ghaemmaghami analyzed data. A. Buchwalter prepared the figures and wrote the manuscript.

Disclosures: The authors declare no competing interests exist.

Submitted: 11 July 2023
Revised: 10 October 2023
Accepted: 27 October 2023

References

Anderson, C.L., E.R. Langer, T.C. Routes, S.F. McWilliams, I. Bereslavskyy, T.J. Kamp, and L.L. Eckhardt. 2021. Most myopathic lamin variants aggregate: A functional genomics approach for assessing variants of uncertain significance. *NPJ Genom. Med.* 6:103. https://doi.org/10.1038/s41525-021-00265-x

Bard, J.A.M., C. Bashore, K.C. Dong, and A. Martin. 2019. The 26S proteasome utilizes a kinetic gateway to prioritize substrate degradation. *Cell*. 177:286–298.e15. https://doi.org/10.1016/j.cell.2019.02.031

Bence, N.F., R.M. Sampat, and R.R. Kopito. 2001. Impairment of the ubiquitin-proteasome system by protein aggregation. *Science*. 292:1552–1555. https://doi.org/10.1126/science.292.5521.1552

Ben-Harush, K., N. Wiesel, D. Frenkiel-Krispin, D. Moeller, E. Soreq, U. Aebi, H. Herrmann, Y. Gruenbaum, and O. Medalia. 2009. The supramolecular organization of the C. elegans nuclear lamin filament. *J. Mol. Biol.* 386:1392–1402. https://doi.org/10.1016/j.jmb.2008.12.024

Beyret, E., H.-K. Liao, M. Yamamoto, R. Hernandez-Benitez, Y. Fu, G. Erikson, P. Reddy, and J.C. Izpisua Belmonte. 2019. Single-dose CRISPR-Cas9 therapy extends lifespan of mice with Hutchinson-Gilford progeria syndrome. *Nat. Med.* 25:419–422. https://doi.org/10.1038/s41591-019-0343-4

Buchwalter, A., and M.W. Hetzer. 2017. Nucleolar expansion and elevated protein translation in premature aging. *Nat. Commun.* 8:328. https://doi.org/10.1038/s41467-017-00322-z

Burke, B., and C.L. Stewart. 2013. The nuclear lamins: Flexibility in function. *Nat. Rev. Mol. Cell Biol.* 14:13–24. https://doi.org/10.1038/nrm3488

Cao, K., B.C. Capell, M.R. Erdos, K. Djabali, and F.S. Collins. 2007. A lamin A protein isoform overexpressed in Hutchinson-Gilford progeria syndrome interferes with mitosis in progeria and normal cells. *Proc. Natl. Acad. Sci. USA*. 104:4949–4954. https://doi.org/10.1073/pnas.0611640104

Chen, Y.R., I. Harel, P.P. Singh, I. Ziv, E. Moses, U. Goshtchevsky, B.E. Machado, A. Brunet, and D.F. Jarosz. 2022. Tissue-specific landscape of protein aggregation and quality control in an aging vertebrate. *biorxiv*. https://doi.org/10.1101/2022.02.26.482120 (Preprint posted February 26, 2022).

Ciryam, P., G.G. Tartaglia, R.I. Morimoto, C.M. Dobson, and M. Vendruscolo. 2013. Widespread aggregation and neurodegenerative diseases are associated with supersaturated proteins. *Cell Rep.* 5:781–790. https://doi.org/10.1016/j.celrep.2013.09.043

D'Angelo, M.A., M. Raices, S.H. Panowski, and M.W. Hetzer. 2009. Age-dependent deterioration of nuclear pore complexes causes a loss of nuclear integrity in postmitotic cells. *Cell*. 136:284–295. https://doi.org/10.1016/j.cell.2008.11.037

Erdos, M.R., W.A. Cabral, U.L. Tavarez, K. Cao, J. Gvozdenovic-Jeremic, N. Narisu, P.M. Zerfas, S. Crumley, Y. Boku, G. Hanson, et al. 2021. A targeted antisense therapeutic approach for Hutchinson-Gilford progeria syndrome. *Nat. Med.* 27:536–545. https://doi.org/10.1038/s41591-021-01274-0

Eriksson, M., W.T. Brown, L.B. Gordon, M.W. Glynn, J. Singer, L. Scott, M.R. Erdos, C.M. Robbins, T.Y. Moses, P. Berglund, et al. 2003. Recurrent de novo point mutations in lamin A cause Hutchinson-Gilford progeria syndrome. *Nature*. 423:293–298. https://doi.org/10.1038/nature01629

Gabriel, D., D. Roedl, L.B. Gordon, and K. Djabali. 2015. Sulforaphane enhances progerin clearance in Hutchinson-Gilford progeria fibroblasts. *Aging Cell*. 14:78–91. https://doi.org/10.1111/acel.12300

Hamczyk, M.R., R. Villa-Bellosta, P. Gonzalo, M.J. Andrés-Manzano, P. Nogales, J.F. Bentzon, C. López-Otín, and V. Andrés. 2018. Vascular smooth muscle-specific progerin expression accelerates atherosclerosis and death in a mouse model of Hutchinson-Gilford progeria syndrome. *Circulation*. 138:266–282. https://doi.org/10.1161/CIRCULATIONAHA.117.030856

Hamczyk, M.R., R. Villa-Bellosta, V. Quesada, P. Gonzalo, S. Vidak, R.M. Nevado, M.J. Andrés-Manzano, T. Misteli, C. López-Otín, and V. Andrés. 2019. Progerin accelerates atherosclerosis by inducing endoplasmic reticulum stress in vascular smooth muscle cells. *EMBO Mol. Med.* 11:e9736. https://doi.org/10.15252/emmm.201809736

Hasper, J., K. Welle, J. Hryhorenko, S. Ghaemmaghami, and A. Buchwalter. 2023. Turnover and replication analysis by isotope labeling (TRAIL) reveals the influence of tissue context on protein and organelle lifetimes. *Mol. Syst. Biol.* 19:e11393. https://doi.org/10.15252/msb.202211393

Hindson, B.J., K.D. Ness, D.A. Masquelier, P. Belgrader, N.J. Heredia, A.J. Makarewicz, I.J. Bright, M.Y. Lucero, A.L. Hiddessen, T.C. Legler, et al. 2011. High-throughput droplet digital PCR system for absolute quantitation of DNA copy number. *Anal. Chem.* 83:8604–8610. https://doi.org/10.1021/ac202028g

Kim, P.H., J. Luu, P. Heizer, Y. Tu, T.A. Weston, N. Chen, C. Lim, R.L. Li, P.-Y. Lin, J.C.Y. Dunn, et al. 2018. Disrupting the LINC complex in smooth muscle cells reduces aortic disease in a mouse model of Hutchinson-Gilford progeria syndrome. *Sci. Transl. Med.* 10:eaat7163. https://doi.org/10.1126/scitranslmed.aat7163

Koblan, L.W., M.R. Erdos, C. Wilson, W.A. Cabral, J.M. Levy, Z.-M. Xiong, U.L. Tavarez, L.M. Davison, Y.G. Gete, X. Mao, et al. 2021. In vivo base editing rescues Hutchinson-Gilford progeria syndrome in mice. *Nature*. 589:608–614. https://doi.org/10.1038/s41586-020-03086-7

Kubben, N., W. Zhang, L. Wang, T.C. Voss, J. Yang, J. Qu, G.-H. Liu, and T. Misteli. 2016. Repression of the antioxidant NRF2 pathway in premature aging. *Cell*. 165:1361–1374. https://doi.org/10.1016/j.cell.2016.05.017

McAlister, G.C., E.L. Huttlin, W. Haas, L. Ting, M.P. Jedrychowski, J.C. Rogers, K. Kuhn, I. Pike, R.A. Grothe, J.D. Blethrow, and S.P. Gygi. 2012. Increasing the multiplexing capacity of TMTs using reporter ion isotopologues with isobaric masses. *Anal. Chem.* 84:7469–7478. https://doi.org/10.1021/ac301572t

McAlister, G.C., D.P. Nusinow, M.P. Jedrychowski, M. Wühr, E.L. Huttlin, B.K. Erickson, R. Rad, W. Haas, and S.P. Gygi. 2014. MultiNotch MS3 enables accurate, sensitive, and multiplexed detection of differential expression across cancer cell line proteomes. *Anal. Chem.* 86:7150–7158. https://doi.org/10.1021/ac502040v

McClatchy, D.B., M.-Q. Dong, C.C. Wu, J.D. Venable, and J.R. Yates III. 2007. 15N metabolic labeling of mammalian tissue with slow protein turnover. *J. Proteome Res.* 6:2005–2010. https://doi.org/10.1021/pr060599n

Merideth, M.A., L.B. Gordon, S. Clauss, V. Sachdev, A.C.M. Smith, M.B. Perry, C.C. Brewer, C. Zalewski, H.J. Kim, B. Solomon, et al. 2008. Phenotype and course of Hutchinson-Gilford progeria syndrome. *N. Engl. J. Med.* 358:592–604. https://doi.org/10.1056/NEJMoa0706898

Nmezi, B., J. Xu, R. Fu, T.J. Armiger, G. Rodriguez-Bey, J.S. Powell, H. Ma, M. Sullivan, Y. Tu, N.Y. Chen, et al. 2019. Concentric organization of A- and B-type lamins predicts their distinct roles in the spatial organization and stability of the nuclear lamina. *Proc. Natl. Acad. Sci. USA*. 116:4307–4315. https://doi.org/10.1073/pnas.1810070116

Olzscha, H., S.M. Schermann, A.C. Woerner, S. Pinkert, M.H. Hecht, G.G. Tartaglia, M. Vendruscolo, M. Hayer-Hartl, F.U. Hartl, and R.M. Vabulas. 2011. Amyloid-like aggregates sequester numerous metastable proteins with essential cellular functions. *Cell*. 144:67–78. https://doi.org/10.1016/j.cell.2010.11.050

Osorio, F.G., C.L. Navarro, J. Cadiñanos, I.C. López-Mejía, P.M. Quirós, C. Bartoli, J. Rivera, J. Tazi, G. Guzmán, I. Varela, et al. 2011. Splicing-directed therapy in a new mouse model of human accelerated aging. *Sci. Transl. Med.* 3:106ra107. https://doi.org/10.1126/scitranslmed.3002847

Peterson, A.C., J.D. Russell, D.J. Bailey, M.S. Westphall, and J.J. Coon. 2012. Parallel reaction monitoring for high resolution and high mass accuracy quantitative, targeted proteomics. *Mol. Cell. Proteomics*. 11:1475–1488. https://doi.org/10.1074/mcp.O112.020131

Puttaraju, M., M. Jackson, S. Klein, A. Shilo, C.F. Bennett, L. Gordon, F. Rigo, and T. Misteli. 2021. Systematic screening identifies therapeutic antisense oligonucleotides for Hutchinson-Gilford progeria syndrome. *Nat. Med.* 27:526–535. https://doi.org/10.1038/s41591-021-01262-4

Quinlivan, E.P., and J.F. Gregory III. 2008. DNA digestion to deoxyribonucleoside: A simplified one-step procedure. *Anal. Biochem.* 373:383–385. https://doi.org/10.1016/j.ab.2007.09.031

Razafsky, D., C. Ward, C. Potter, W. Zhu, Y. Xue, V.J. Kefalov, L.G. Fong, S.G. Young, and D. Hodzic. 2016. Lamin B1 and lamin B2 are long-lived proteins with distinct functions in retinal development. *Mol. Biol. Cell.* 27:1928–1937. https://doi.org/10.1091/mbc.e16-03-0143

Reddel, C.J., and A.S. Weiss. 2004. Lamin A expression levels are unperturbed at the normal and mutant alleles but display partial splice site selection in Hutchinson-Gilford progeria syndrome. *J. Med. Genet.* 41:715–717. https://doi.org/10.1136/jmg.2004.019323

Rivera-Torres, J., R. Acín-Perez, P. Cabezas-Sánchez, F.G. Osorio, C. Gonzalez-Gómez, D. Megias, C. Cámara, C. López-Otín, J.A. Enríquez, J.L. Luque-García, and V. Andrés. 2013. Identification of mitochondrial dysfunction in Hutchinson-Gilford progeria syndrome through use of stable isotope labeling with amino acids in cell culture. *J. Proteomics.* 91: 466–477. https://doi.org/10.1016/j.jprot.2013.08.008

Santiago-Fernández, O., F.G. Osorio, V. Quesada, F. Rodríguez, S. Basso, D. Maeso, L. Rolas, A. Barkaway, S. Nourshargh, A.R. Folgueras, et al. 2019. Development of a CRISPR/Cas9-based therapy for Hutchinson-Gilford progeria syndrome. *Nat. Med.* 25:423–426. https://doi.org/10.1038/s41591-018-0338-6

Sapra, K.T., Z. Qin, A. Dubrovsky-Gaupp, U. Aebi, D.J. Müller, M.J. Buehler, and O. Medalia. 2020. Nonlinear mechanics of lamin filaments and the meshwork topology build an emergent nuclear lamina. *Nat. Commun.* 11: 6205. https://doi.org/10.1038/s41467-020-20049-8

Scaffidi, P., and T. Misteli. 2005. Reversal of the cellular phenotype in the premature aging disease Hutchinson-Gilford progeria syndrome. *Nat. Med.* 11:440–445. https://doi.org/10.1038/nm1204

Scaffidi, P., and T. Misteli. 2006. Lamin A-dependent nuclear defects in human aging. *Science.* 312:1059–1063. https://doi.org/10.1126/science.1127168

Schreiber, K.H., and B.K. Kennedy. 2013. When lamins go bad: Nuclear structure and disease. *Cell.* 152:1365–1375. https://doi.org/10.1016/j.cell.2013.02.015

Su, D., C.T.Y. Chan, C. Gu, K.S. Lim, Y.H. Chionh, M.E. McBee, B.S. Russell, I.R. Babu, T.J. Begley, and P.C. Dedon. 2014. Quantitative analysis of ribonucleoside modifications in tRNA by HPLC-coupled mass spectrometry. *Nat. Protoc.* 9:828–841. https://doi.org/10.1038/nprot.2014.047

Swift, J., I.L. Ivanovska, A. Buxboim, T. Harada, P.C.D.P. Dingal, J. Pinter, J.D. Pajerowski, K.R. Spinler, J.-W. Shin, M. Tewari, et al. 2013. Nuclear lamin-A scales with tissue stiffness and enhances matrix-directed differentiation. *Science.* 341:1240104. https://doi.org/10.1126/science.1240104

Toyama, B.H., J.N. Savas, S.K. Park, M.S. Harris, N.T. Ingolia, J.R. Yates III, and M.W. Hetzer. 2013. Identification of long-lived proteins reveals exceptional stability of essential cellular structures. *Cell.* 154:971–982. https://doi.org/10.1016/j.cell.2013.07.037

Varga, R., M. Eriksson, M.R. Erdos, M. Olive, I. Harten, F. Kolodgie, B.C. Capell, J. Cheng, D. Faddah, S. Perkins, et al. 2006. Progressive vascular smooth muscle cell defects in a mouse model of Hutchinson-Gilford progeria syndrome. *Proc. Natl. Acad. Sci. USA.* 103:3250–3255. https://doi.org/10.1073/pnas.0600012103

Vidak, S., L.A. Serebryannyy, G. Pegoraro, and T. Misteli. 2023. Activation of endoplasmic reticulum stress in premature aging via the inner nuclear membrane protein SUN2. *Cell Rep.* 42:112534. https://doi.org/10.1016/j.celrep.2023.112534

Wang, D., B. Eraslan, T. Wieland, B. Hallström, T. Hopf, D.P. Zolg, J. Zecha, A. Asplund, L.H. Li, C. Meng, et al. 2019. A deep proteome and transcriptome abundance atlas of 29 healthy human tissues. *Mol. Syst. Biol.* 15:e8503. https://doi.org/10.15252/msb.20188503

Welle, K.A., T. Zhang, J.R. Hryhorenko, S. Shen, J. Qu, and S. Ghaemmaghami. 2016. Time-resolved analysis of proteome dynamics by tandem mass tags and stable isotope labeling in cell culture (TMT-SILAC) hyperplexing. *Mol. Cell. Proteomics.* 15:3551–3563. https://doi.org/10.1074/mcp.M116.063230

Supplemental material

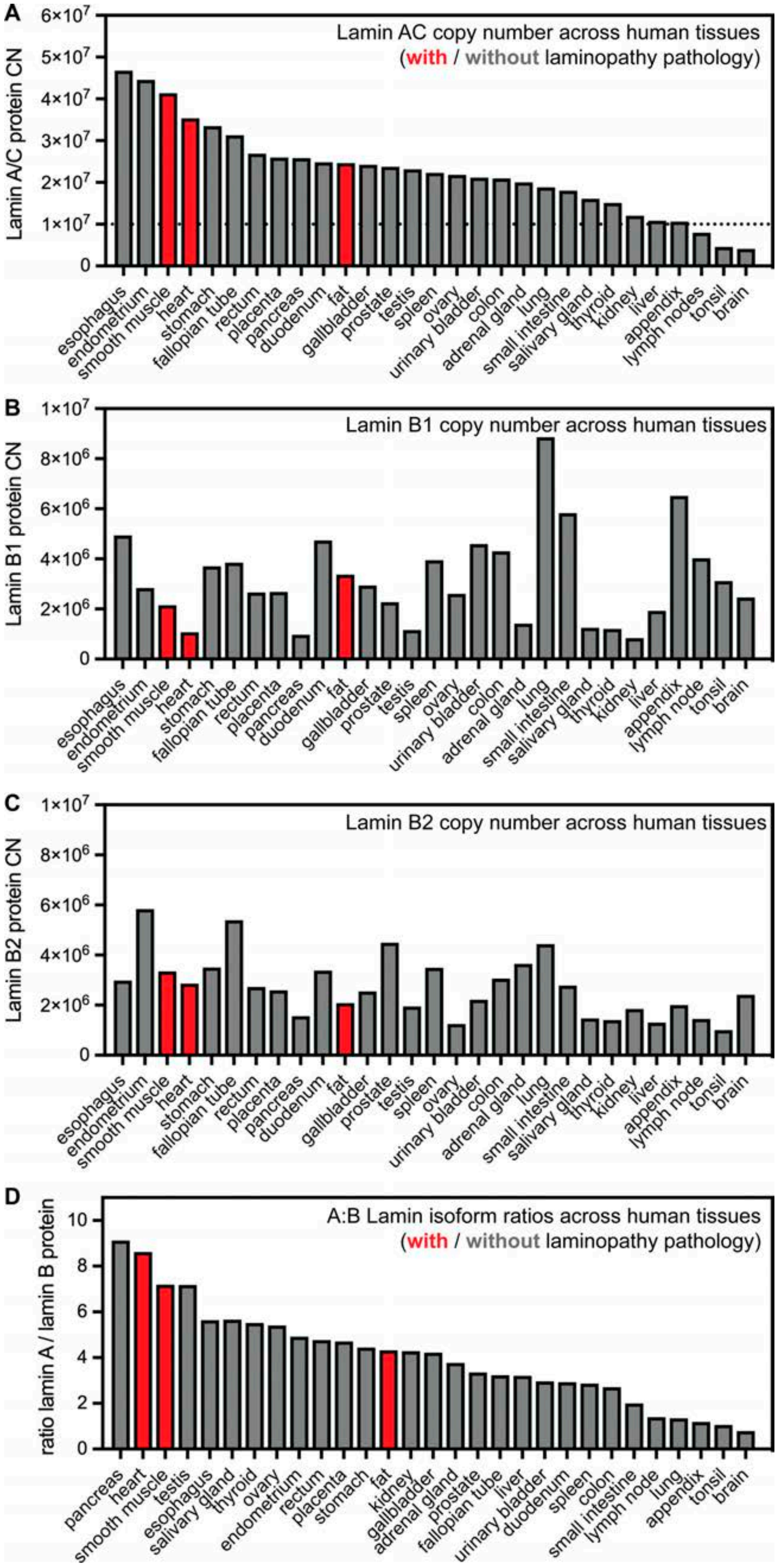

Figure S1. **Lamin protein abundance comparisons across human tissues. (A–C)** Estimated copy number per cell of lamin A/C (A), lamin B1 (B), and lamin B2 (C) across human tissues, determined by histone normalization ("proteomic ruler" method). **(D)** Abundance ratio of A-type (lamin A/C) to B-type (lamin B1 and B2) lamin proteins across human tissues. All data are reanalyzed from Wang et al. (2019).

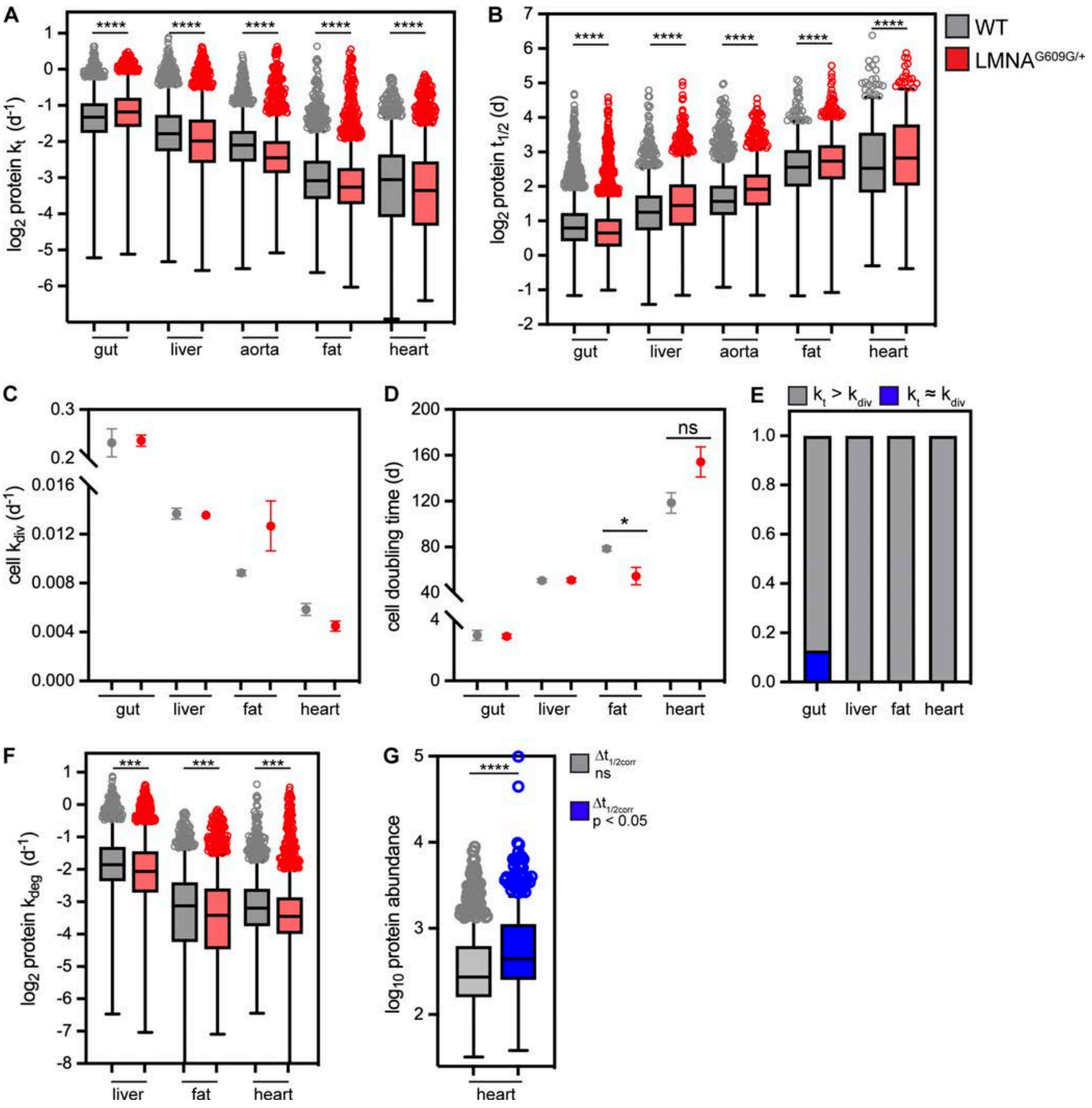

Figure S2. **Protein and cell turnover parameters in healthy and progeroid tissues. (A and B)** Protein turnover rates (k_t) (A) and predicted half-lives ($t_{1/2}$) (B) for proteins in tissues of healthy (gray) and progeroid (red) animals. These values are significantly different across tissues ($P < 0.0001$ for each genotype by Kruskal–Wallis test) and across genotypes ($P < 0.0001$ by Mann–Whitney test for each tissue). Box (Tukey) plot center line indicates median; box limits indicate 25th to 75th percentiles; whiskers indicate 1.5× interquartile range; points indicate outlier values. **(C and D)** Cell division rates (k_{div}) (C) and predicted cell doubling times (D) determined by TRAIL for tissues in healthy (gray) and progeroid (red) animals. Bars indicate standard error of the mean. * indicates that cell turnover rate is significantly faster in progeroid fat ($P < 0.05$, unpaired t test). **(E)** Only the proliferative intestine has a significant number of proteins whose k_t is equal to or lesser than k_{div}, suggesting that these proteins are diluted by cell division. **(F)** Cell cycle–corrected protein degradation rates (k_{deg}) determined for proteins in liver, fat, and heart muscle. *** indicates a significant decrease in protein turnover flux in progeroid tissues ($P < 0.001$, Mann–Whitney test). Data from wild-type animals reproduced from Hasper et al. (2023). **(G)** Comparison of protein abundance in progeroid tissues between proteins with significantly altered lifetime in progeroid tissue (blue) versus proteins with unchanged lifetime in progeroid tissue (gray). Tukey plot. **** indicates that proteins with impaired turnover in progeroid tissue are more abundant than proteins with unchanged turnover in progeroid tissue (****, $P < 0.0001$ by Mann–Whitney test).

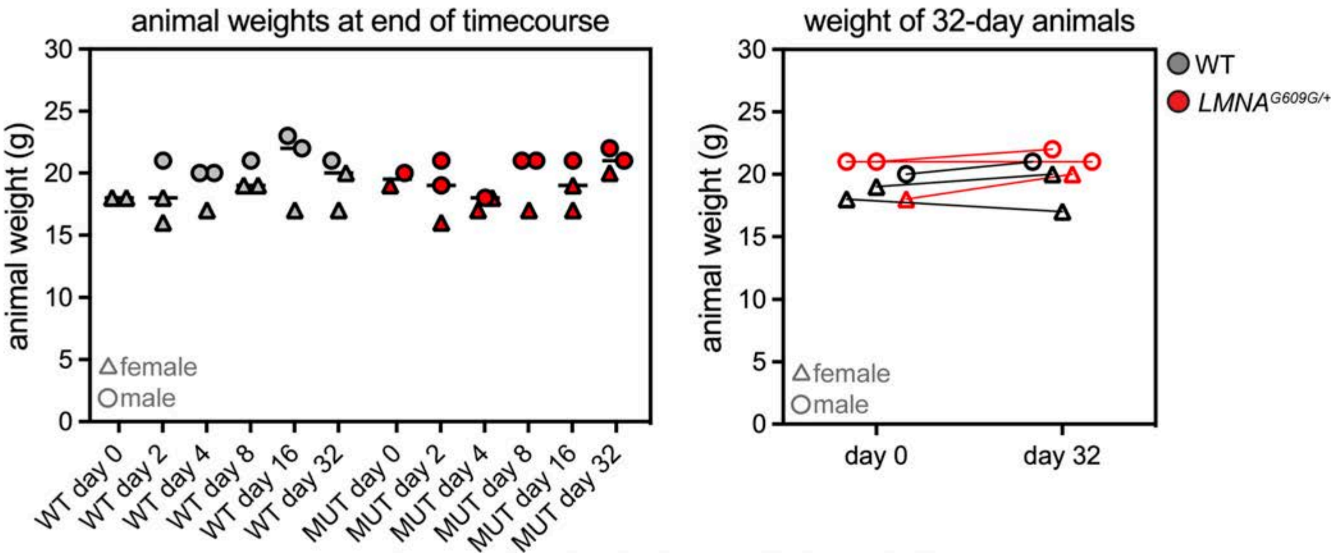

Figure S3. **Wild-type and progeroid animal weights remained stable throughout TRAIL timecourse. (A)** Balanced mixtures of male and female mice were used for labeling time course. Weights of animals used for all time points of metabolic labeling are consistent and are not significantly different at any time point (ns, $P > 0.05$, one-way ANOVA for each genotype). **(B)** Comparison of the weights of the same animals at the beginning and end of the 32-d time course shows no change.

Provided online are Table S1, Table S2, and Table S3. Table S1 list contains protein turnover data in wild-type and progeroid mouse tissues. Table S2 list reports cell turnover data in wild-type and progeroid mouse tissues. Table S3 list contains isotope enrichment measurements for lamin A and progerin peptides in 15N-labeled progeroid mouse tissue used in this study.